Bioorganic Chemistry 94 (2020) 103432

Contents lists available at ScienceDirect

Bioorganic Chemistry

journal homepage: www.elsevier.com/locate/bioorg

Synthesis of naphthalimide-carborane and metallacarborane conjugates: Anticancer activity, DNA binding ability

Jan Nekvinda[a,b], Daria Różycka[c,1], Sebastian Rykowski[c,1], Eliza Wyszko[d,*], Agnieszka Fedoruk-Wyszomirska[d], Dorota Gurda[d], Marta Orlicka-Płocka[d], Małgorzata Giel-Pietraszuk[d], Agnieszka Kiliszek[d], Wojciech Rypniewski[d], Rafał Bachorz[c], Jakub Wojcieszak[e], Bohumir Grüner[a], Agnieszka B. Olejniczak[c,*]

[a] Institute of Inorganic Chemistry, Academy of Sciences of the Czech Republic, v.v.i., Hlavní 1001, CZ-250 68 Řež, Czech Republic
[b] Department of Organic Chemistry, Faculty of Sciences, Charles University, Hlavova 2030, 128 42 Prague 2, Czech Republic
[c] Institute of Medical Biology, Polish Academy of Sciences, 106 Lodowa St., Lodz 93-232, Poland
[d] Institute of Bioorganic Chemistry, Polish Academy of Sciences, 12/14 Z. Noskowskiego St., 61–704 Poznan, Poland
[e] Department of Pharmacodynamics, Medical University of Lodz, 1 Muszynskiego St., 90-151 Lodz, Poland

ARTICLE INFO

Keywords:
Naphthalimides
Carborane
Metallacarborane
Anticancer activity

ABSTRACT

The development of 1,8-naphthalimide derivatives as DNA-targeting anticancer agents is a rapidly growing area and has resulted in several derivatives entering into clinical trials. One of original recent developments is the use of boron clusters: carboranes and metallacarboranes in the design of pharmacologically active molecules. In this direction several naphthalimide-carborane and metallacarborane conjugates were synthesized in the present study. Their effect on a cancer cell line – cytotoxicity, type of cell death, cell cycle, and ROS production were investigated. The tested conjugates revealed different activities than the leading members of the naphthalimides family, namely mitonafide and pinafide. These derivatives could induce G0/G1 arrest and promote mainly apoptosis in HepG2 cell line. Our investigations demonstrated that the most promising molecule is *N*-{[2-(3,3′-commo-bis(1,2-dicarba-3-cobalta(III)-*closo*-dodecaborate-1-yl)ethyl]-1′-aminoethyl)}-1,8-naphthalimide] (**17**). It was shown that **17** exhibited cytotoxicity against HepG2 cells, activated cell apoptosis, and caused cell cycle arrest in HepG2 cells. Further investigations in HepG2 cells revealed that compound **17** can also induce ROS generation, particularly mitochondrial ROS (mtROS), which was also proved by increased 8-oxo-dG level in DNA. Additionally to biological assays the interaction of the new compounds with ct-DNA was studied by CD spectra and melting temperature, thus demonstrating that these compounds were rather weak classical DNA intercalators.

1. Introduction

Naphthalimides (IUPAC name: 1H-benzo[*de*]isoquinoline-1,3-(2H)-diones) are the class of polycyclic imides consisting of π-deficient flat aromatic or heteroaromatic ring systems. These compounds and their derivatives exhibit advantageous physicochemical and biological properties. Most of the naphthalimides are fluorescent and exhibit a broad range of biological properties such as anticancer, antibacterial, antiviral, and analgesic effects [1]. 1,8-Naphthalimides are substances that exhibit high antitumor activities and have potential abilities to suppress tumor growth and metastasis usually based on intercalation into DNA [2]. Meanwhile, naphthalimides or the derivatives exert their anticancer activities through other multiple ways such as induction of reactive oxygen species (ROS) and malfunction of lysosome and mitochondria [3], inhibition of histone deacetylase [4], DNA and RNA synthesis [5], receptor tyrosine kinases [6]. Three leading members of this family are: mitonafide (3-nitro-*N*-(2-dimethylaminoethyl)-1,8-naphthalimide), pinafide (3-nitro-*N*-(2-(1-pyrrolidinyl)ethyl)-1,8-naphthalimide) and amonafide (3-amino-*N*-(2-dimethylaminoethyl)-1,8-naphthalimide) (Fig. 1). Mitonafide has entered the clinical trial stage for the treatment of solid tumors and has exhibited excellent antitumor activity; however, other 1,8-naphthalimide derivatives are characterized by various adverse physicochemical properties, high toxicity, poor pharmacokinetics, and other drawbacks [7]. Extensive efforts,

* Corresponding authors.
E-mail addresses: wyszkoe@ichb.poznan.pl (E. Wyszko), aolejniczak@cbm.pan.pl (A.B. Olejniczak).
[1] Equal contribution.

https://doi.org/10.1016/j.bioorg.2019.103432
Received 20 August 2019; Received in revised form 11 October 2019; Accepted 10 November 2019
Available online 19 November 2019

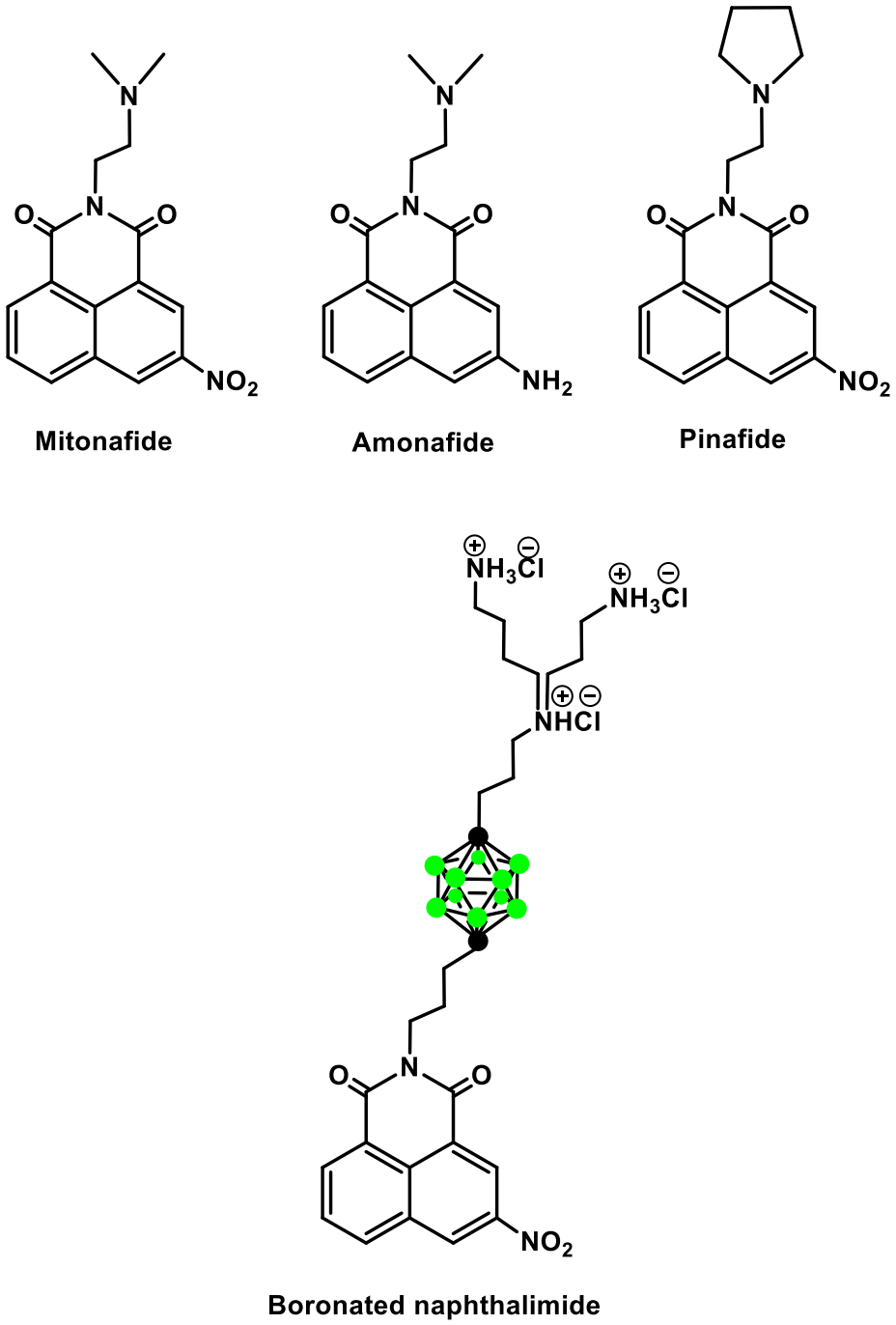

Fig. 1. Structures of mitonafide, amonafide, pinafide, and boronated naphthalimide.

including the modification of the side chain, the aromatic ring system, and the substituents on the ring, have been made to search for more selective naphthalimide derivatives to improve their potency and reduce side effects [8–10]. The structure–activity relationships of 1,8-naphthalimide derivatives were summarized by Tomczyk et al. [11]. Many efforts have been focused on the modification of imide (effect on binding strength with DNA and chain length influences the activity; presence of metal complexes increase cytotoxicity and affords better affinity with DNA) and positions 3 and 4 of the ring (heterocyclic substituent increases intercalation with DNA, and the activity depends upon substitution of heterocycles).

Although boron, in the form of boric acid, has been used as a mild antiseptic and eye wash since the 19th century [12], its use in drug design is a new frontier in medicinal chemistry [12,13]. The bortezomib is an example success story in the field of designing new boron containing drugs.

We proposed to use dicarba-*closo*-dodecaboranes (carborane, $C_2B_{10}H_{12}$), and metallacarboranes (a sandwich of two $(C_2B_9H_{11})_2^-$ clusters with a metal ion coordinated in the center) for modification of naphthalimide. The biomedical application of carboranes has been reviewed over the years [14–19], focusing mainly on their application as boron carriers in boron neutron capture therapy (BNCT) and as surrogates for heterocycles, annulated carbon rings, or most popularly, for substituted or unsubstituted phenyl ring. Metallacarboranes are known inhibitors of Human Immunodeficiency Virus (HIV) protease [20,21]. The recent appeal of boron clusters for the pharmaceutical industry lies in the knowledge that these clusters are abiotic and therefore chemically and biologically orthogonal to native cellular components. In

addition, the unique interaction properties of boron clusters and their derivatives with biomolecules, differ than those between carbon-based molecules offering novel features in potential drug targeting. Furthermore, the properties of boron clusters that are useful in drug design include the following lipophilicity, amphiphilicity or hydrophobicity, chemical stability and simultaneous susceptibility to functionalization, spherical or ellipsoidal geometry and rigid 3D arrangement.

Ghaneolhosseini and Sjöberg have described synthesis of a boronated naphthalimide (Fig. 1) based on mitonafide and DMP 840 ((R,R) 2,2′-[1,2-ethanediylbis[imino(1-methyl-2.1-ethanediyl)]-bis(5-nitro 1H-benz[*de*]-isoquinoline-1,3-2H) dione] dimethanesulfonate) with special attention devoted to boron neutron capture therapy (BNCT). The synthesis of a water-soluble naphthalimide derivative containing both *para*-carboranyl and spermidine moieties was carried out knowing that the nitro or amino substituents on the chromophore rings are essential for antitumor activity and DNA binding; however, the DNA-binding capacity of the conjugate has not been reported [22].

Motivated by promising antitumor activities of naphthalimide and bearing in mind properties of boron clusters, we decided to synthesize *N*-carboranyl/metallacarboranyl naphthalimide analogs substituted with dicarba-*closo*-dodecaborane (*ortho*-, *meta*-, and *para*-isomer) and metallacarborane (containing cobalt or chromium ion) in order to assess the effect of boron clusters on their biological activity, including anticancer activity, apoptosis/necrosis induction, ROS production, or effect on cell cycle. Calf thymus DNA (ct-DNA) studies were also performed to evaluate their interaction with DNA.

2. Results and discussion

2.1. Chemistry

2.1.1. Synthesis of naphthalimide-boron cluster conjugates

The newly synthesized naphthalimide derivatives containing boron clusters, namely carboranes (**3**, **5**, **7**) and metallacarboranes (**9**, **11**, **13**, **15**, **17**, **18**), were obtained in a simple one-step procedure that used nucleophilic reaction of the corresponding boron cluster-based amine donors of various structures [23–27] with 3-nitro-1,8-naphthalic anhydride (**1**). This provided the expected substitution in good yields after a simple work-up (Schemes 1–3).

The selected amine **2**, **4**, **6**, **8**, **10**, **12**, **14,** or **16**, dissolved in absolute ethanol, was added to a suspension of 3-nitro-1,8-naphthalic anhydride (**1**) in the same solvent.

Herein, we describe the synthesis of naphthalimide analogs bearing *ortho*-and *meta*-carboranes, and bulkier and more hydrophobic metallacarborane groups that have not been reported previously. The yield of the products **3**, **5**, **7**, **9**, **11**, **13**, **15**, **17**, and **18** after isolation and purification by column chromatography varied between 7% and 75%, depending on the amine boron cluster type, with the lowest yield for compound **17** due to preferential formation of disubstituted product **18**, which was isolated in 62% yield. Compounds **13, 15, 17,** and **18** are asymmetric, due to asymmetric position(s) of the substituents at carbon atom(s), and are thus protochiral. The products **3**, **5**, **7**, **9**, **11**, **13**, **15**, **17**, and **18** were characterized by ^{1}H, ^{13}C, ^{11}B NMR, FT-IR, MS, (Figs. S1–S41 (ESI)), and TLC.

2.1.2. X-ray structure analysis

The structure of **5** contained two molecules per asymmetric unit and a significant number of disordered solvent molecules (Fig. 2A). The solvent was observed as strong peaks of electron density that could not be interpreted, thus forming a distinct solvent channel. SQUEEZE [28] was used to model the disordered solvent amounting to 16% of the crystal volume and 320 electrons per unit cell. The R-factor decreased from 13% before modeling the disordered solvent to 7.7% after refinement. After further refinement with SHELXL, the R-factor decreased to the final value of 0.0562. Refinement of the ordered atoms was unrestrained, except for hydrogen atoms that were maintained at riding positions (Fig. 2B).

In the structure of **5**, the boron clusters pack into layers in which bundles of four columns formed by the clusters are separated by channels of disordered solvent. The naphthalimide rings also pack together in layers in which the rings are parallel to each other and stack into columns. The nitro groups of neighboring **5** molecules come into contact. The groups are aligned parallel to each other; one of the nitrogen atoms is 2.98 Å from the oxygen atom of the other group, while another nitrogen atom makes a symmetric contact with the oxygen atom of the first group. In addition, the oxygen of the nitro groups interact on the other side with one of the carbonyl oxygen atoms of another neighboring molecule (2.79 Å).

The crystal structure of **7** contains one molecule in the asymmetric unit (Fig. 2C). The structure shows static disorder, with a minor conformation of the naphthalimide ring at 180° to the main conformation. Weak but distinct peaks were observed for the minor conformation in the electron density map. The occupancy factor for the minor conformation was refined to 0.0662. Refining the minor conformation was problematic due to weak electron density and partial overlapping with the major conformation. Subsequently, geometric restraints and constraints were imposed on the minor conformation to maintain it in reasonable geometry. Other atoms were refined unrestrained, except for hydrogen atoms that were maintained in their riding positions (Fig. 2D).

In the structure of **7**, the boron clusters also pack together forming distinct layers in the crystal lattice. The naphthalimide rings pack together in layers formed by parallel pairs, staggered at approximately 40° to each other. The nitrogen atom of the nitro group is 2.92 Å from a carbonyl oxygen of a neighboring, symmetry-related molecule. In the other independent molecule observed in the structure of **7**, the nitrogen atom of the nitro group is 3.12 Å from an oxygen atom of a nitro group from a symmetry-related molecule. Oxygen atoms of the neighboring nitro groups are even closer at 3.04 Å. Table S1 (ESI) summarizes the crystallographic data.

2.2. Biological investigation

2.2.1. In vitro cytotoxic activity

The *in vitro* antitumor activities of the target compounds were evaluated by examining their cytotoxic effects using MTT tetrazolium dye assay [29,30] against two human cancer cell lines, namely HepG2 cells established from hepatocellular carcinoma and RPMI 2650 cells established from squamous cell carcinoma, and their effects were compared with those of mitonafide and pinafide. The IC_{50} values represented the drug concentration (μM) required to inhibit cell growth by 50%, and the results are summarized in Table 1. Generally, naphthalimides containing carborane cluster (**3**, **5**, and **7**) were more cytotoxic than naphthalimides modified with metallacarboranes (**9**, **11**, **13**, **15**, and **17**). Comparison of the activities of the naphthalimides in the series revealed that the presence of lipophilic *para*-carborane group enhances cytotoxic activity. Compound **7** was the most cytotoxic to the tested tumor cell lines at concentration as low as 2.80 μM, particularly being effective for RPMI 2650 cells. Its activity was close to that of pinafide for the same cell line. Conjugate **5** containing *meta*-carborane was slightly less active and showed cytotoxic effects on both cell lines (IC_{50} = 7.84 and 7.03 μM). The presence of *ortho*-carborane cluster in compound **3** resulted in the decrease of activity for RPMI 2650 cells compared to compounds **5** and **7**, but an increase activity for HepG2 cells compared to compound **5**. We hypothesized that the higher activity of conjugate **7**, as compared to conjugates **3** and **5** against both cell lines could be attributable to the different lipophilicity of *ortho*-/*meta*-/*para*-carborane. The lipophilicity of carborane isomers increases in the following order: *ortho*-carborane < *meta*-carborane < *para*-carborane. The high lipophilicity of carboranes and their derivatives can be explained by the presence of a partial negative charge located on boron-bound hydrogen atoms in BH groups and their “hydride-like”

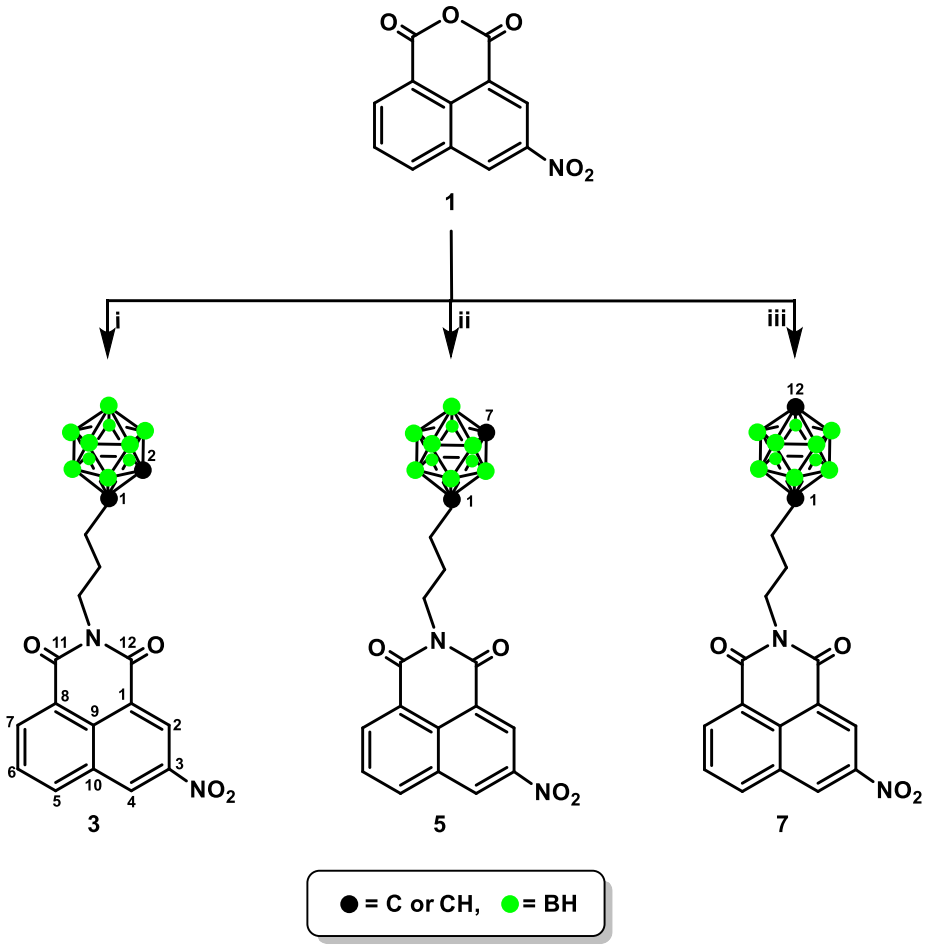

Scheme 1. Synthesis of naphthalimide modified with 1-(3-aminopropyl)-carboranes: 1,2-dicarba-*closo*-dodecaborane (**3**), 1,7-dicarba-*closo*-dodecaborane (**5**), 1,12-dicarba-*closo*-dodecaborane (**7**): (i) 1,2-$C_2B_{10}H_{11}$-$(CH_2)_3NH_2$HCl (**2**), TEA, EtOH, 6 h, 65 °C, 64%; (ii) 1,7-$C_2B_{10}H_{11}$-$(CH_2)_3NH_2$HCl (**4**), TEA, EtOH, 6 h, 65 °C, 73%; (iii) 1,12-$C_2B_{10}H_{11}$-$(CH_2)_3NH_2$HCl (**6**), TEA, EtOH, 6 h, 65 °C, 75%.

character. This prevents them from forming classical hydrogen bonds, which imbues the boron cluster with lipophilic character [16].

Among naphthalimides containing metallacarborane modification (**9**, **11**, **13**, **15**, and **17**), the most active were compounds **13** and **17** bearing metallacarborane containing cobalt ion with IC_{50} = 22.20 and 29.10 μM, respectively, for HepG2 cells. For the same cell line, compound **15** was less active with IC_{50} = 46.21 μM. Compound **11** modified with metallacarborane containing chromium ion showed moderate cytotoxicity against RPMI 2650 cells (IC_{50} = 43.08 μM), while naphthalimides **13** and **15** were not toxic (IC_{50} > 100 μM). Compound **9** was inactive (IC_{50} > 100 μM) against HepG2 and RPMI 2650 cells.

2.2.2. Apoptosis/necrosis assay by flow cytometry

In addition to cell toxicity, we determined the type of cell death that is induced in response to analyzed compounds. Apoptosis and necrosis are the two major processes that lead to cell death. It has been reported that analog NPC-16 (naphthalimide-polyamine conjugate) induced apoptosis and autophagy in HepG2 and Bel-7402 cells [31]. Furthermore, some novel naphthalimide derivatives induced tumor cell apoptosis through lysosomal membrane permeabilization [32].

To investigate whether the tested compounds induce apoptosis in HepG2 cells, we performed flow cytometric analysis by YO-PRO-1/PI dual staining after 24 h incubation of cells with **3**, **5**, **7**, **9**, **11**, **13**, **15**, **17** and **18**. The chosen concentration of each compound corresponded to half of the IC_{50} and whole IC_{50} values. Mitonafide and pinafide were tested as a reference compounds. The results indicate that the analyzed naphthalimide-boron cluster derivatives promote mainly apoptosis in a dose-dependent manner (Figs. 3, S42 (ESI)). Compounds containing metallacarborane modification connected by alkane linker **13** (10 and 20 μM), **15** (20 and 40 μM), and **17** (15 and 30 μM) induce early apoptosis (expressed as percentage of apoptotic cells) as the concentration increases (from 42.13% to 58.68%, 32.77% to 42.29%, and 15.57% to 22.37%, respectively) with only few late apoptotic cells at the highest concentration. Incubation with **3** (3 and 6 μM) and **5** (4 and 8 μM) modified with *ortho*- or *meta*-carborane group, respectively, induces mainly early stages of apoptosis with a moderate level of late apoptosis (from 2.75% to 3.01%, 3.13% to 11.74%, respectively) which increases with concentration. Compounds **7** (2 and 4 μM), **9** (50 and 100 μM), and **11** (50 and 100 μM) induce more rapid cell death, where numerous cells undergo late apoptosis (**7**) and necrosis (**9**, **11**). Compound **18** precipitated, thereby impeding its correct apoptosis/necrosis assessment.

2.2.3. Cell cycle analysis by flow cytometry

Cell cycle disorders such as arrest might be an important cause of cancer cell growth inhibition and consequently loss of cell viability [33]. To shed light on the mechanism responsible for the inhibitory activity of the compounds on cellular viability, we sought to examine the cell cycle regulation. HepG2 cells were exposed to compound **3** (3 and 6 μM), **5** (4 and 8 μM), **7** (2 and 4 μM), **9** (50 and 100 μM), **11** (50 and 100 μM), **13** (10 and 20 μM), **15** (20 and 40 μM), and **17** (15 and 30 μM) for 24 h. The chosen concentration of each compound corresponded to half of the IC_{50} and whole IC_{50} values. Compound **18** precipitated, thus impeding its correct cell cycle analysis assessment.

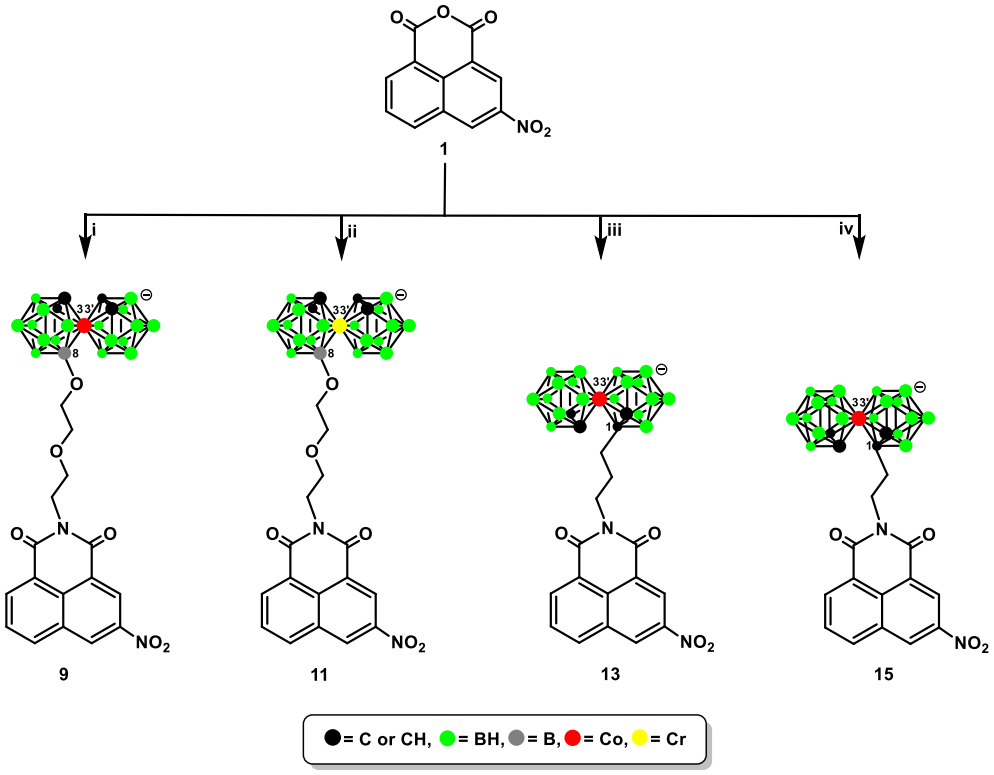

Scheme 2. Synthesis of naphthalimide modified with metallacarborane containing cobalt **9**, **13**, and **15** or chromium **11**: (i) [8-(5-NH_3-$(OCH_2CH_2)_2$-3,3′-Co(1,2-$C_2B_9H_{10}$)(1′,2′-$C_2B_9H_{11}$)]$^-$ (**8**), 5 h, 60 °C, 58%; (ii) [8-(5-NH_3-$(OCH_2CH_2)_2$-3,3′-Cr(1,2-$C_2B_9H_{10}$)(1′,2′-$C_2B_9H_{11}$)]$^-$ (**10**), 5 h, 60 °C, 45%; (iii) [(1-NH_2-$(CH_2)_3$-3,3′-Co(1,2-$C_2B_9H_{10}$)(1′,2′-$C_2B_9H_{11}$)]Me_4N (**12**), 5 h, 60 °C, 37%; (iv) [(1-NH_2-$(CH_2)_2$-3,3′-Co(1,2-$C_2B_9H_{10}$)(1′,2′-$C_2B_9H_{11}$)]Me_4N (**14**), 5 h, 60 °C, 57%.

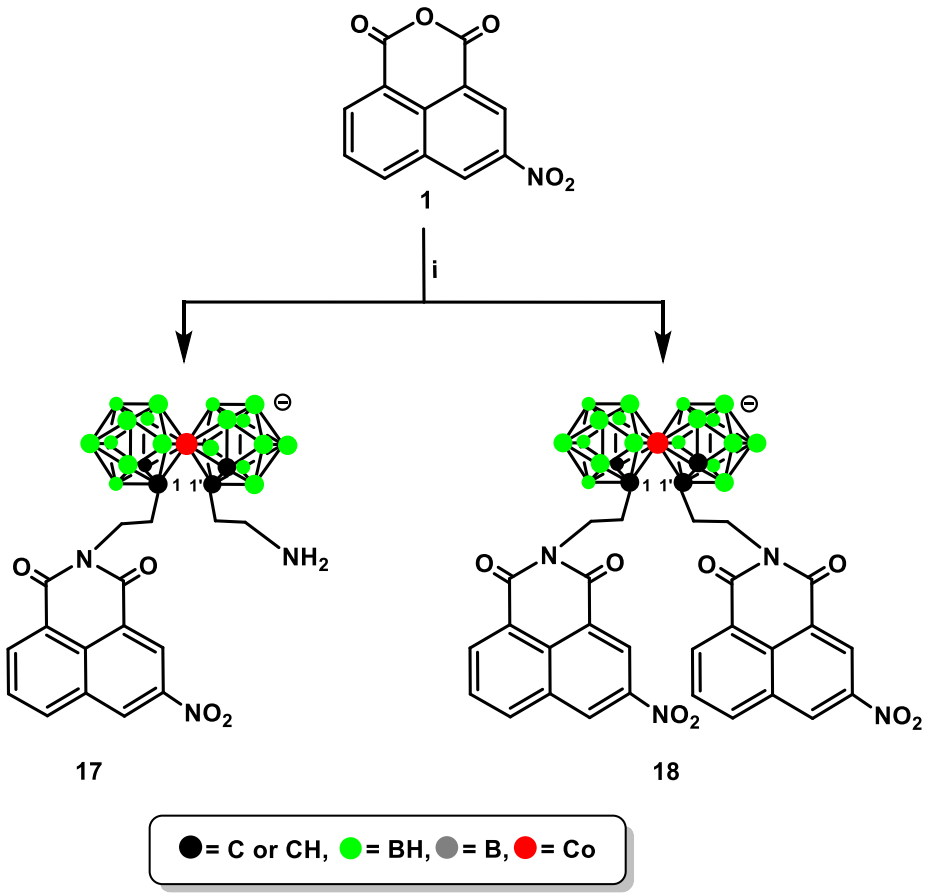

Scheme 3. Synthesis of naphthalimide **17** and bisnaphthalimide **18** bearing metallacarborane: (i) [(1,1′-$(NH_2$-$(CH_2)_2$-3,3′-Co(1,2-$C_2B_9H_{10}$)(1′,2′-$C_2B_9H_{10}$)]Me_4N (**16**), 5 h, 60 °C, 7% for **17**, 62% for **18**.

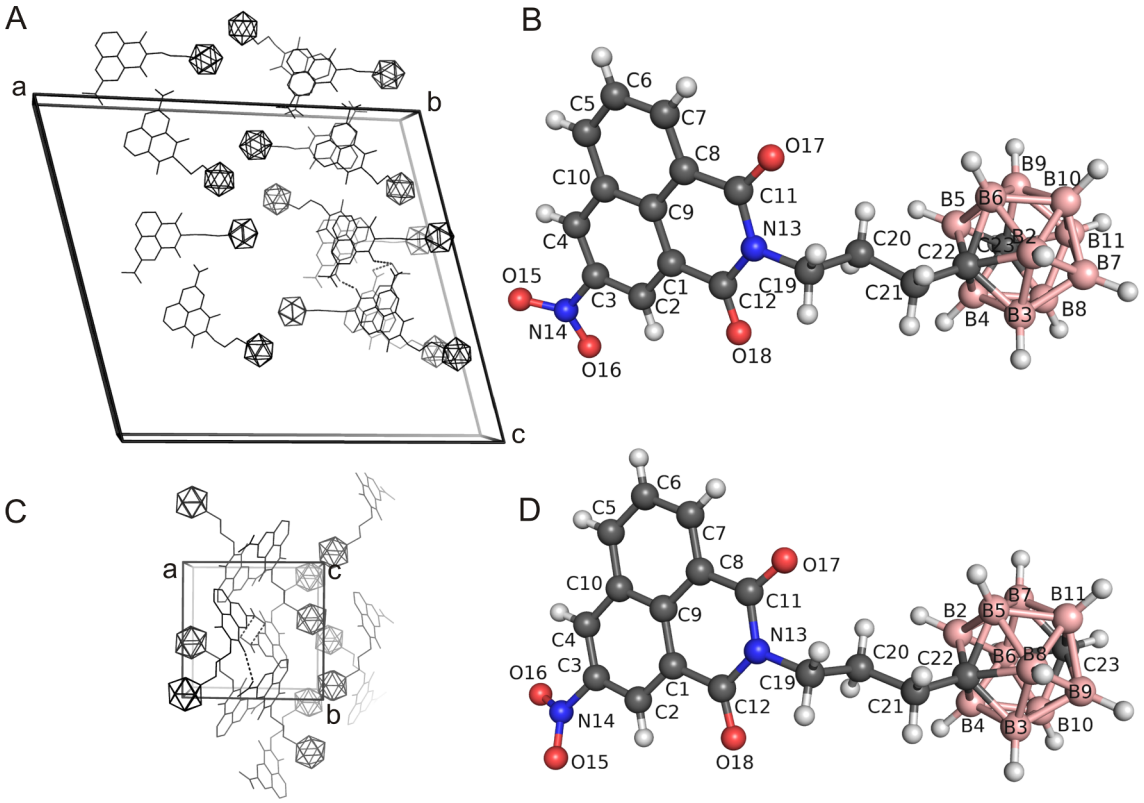

Fig. 2. The crystal packing (A) and a ball-and-stick representation (B) of conjugate *N*-(1,7-carboran-1-yl)-1,8-naphthalimide (**5**); the crystal packing (C) and a ball-and-stick representation (D) of conjugate *N*-(1,12-carboran-1-yl)-1,8-naphthalimide (**7**).

Table 1
Cellular cytotoxic activity of compounds **3**, **5**, **7**, **9**, **11**, **13**, **15**, **17**.

Compound	Cell line, IC_{50}[a][μM]	
	HepG2	RPMI 2650
3	5.95 ± 0.075	28.94 ± 0.087
5	7.84 ± 0.040	7.03 ± 0.016
7	3.54 ± 0.038	2.80 ± 0.020
9	> 100	> 100
11	> 100	43.08 ± 0.065
13	22.2 ± 0.551	> 100
15	46.21 ± 0.030	> 100
17	29.10 ± 0.016	77.47 ± 0.165
18	*	*
pinafide	1.23 ± 0.145	1.68 ± 0.040
mitonafide	< 1	1.42 ± 0.018

[a] Compound concentration required to inhibit tumor cell growth by 50%.
* Precipitation impeding correct viability assessment.

Mitonafide and pinafide were tested as a reference compounds. Subsequently, the cells were examined by flow cytometry, and DNA contents was measured by PI staining. DNA contents analysis revealed that the analyzed compounds exerted different effects than mitonafide and pinafide that arrest cell cycle in the S and G2M phases, respectively (Fig. 4, Fig. S43 (ESI)). Each naphthalimide-boron cluster conjugates affected the cell cycle by increasing the percentage of cells in G0/G1, with increasing concentrations, up to 65.15% followed by a decrease in the number of cells in the G2M phase (up to 5.26% for compound **17**) compared to control. Accumulation of cells in the G0/G1 phase delayed the progression of cell cycle and entry into the S phase; this could be the mechanism of DNA damage by the tested compounds.

Previous studies showed that many drugs induced cell rounding and G2M cell cycle arrest in cancer cells [34]. However, 1,8-naphthalimide derivatives containing Rh(I) and Ru(III) *N*-heterocyclic carbene (NHC) ligands revealed a G1 arrest in response to treatment. Although all obtained compounds caused a significant increase in the G1 phase cell population as compared to 0.1% DMSO, this effect was found to be more pronounced for the Rh(I) analog, followed by the metal-free ligand, and finally the Ru(II) complex [35].

2.2.4. Oxidative stress measurements in HepG2 cells by flow cytometry

It has been proposed that one of the mechanisms by which naphthalimides and their derivatives induce cell cycle arrest and apoptosis in cancer cells is the induction of production of ROS; this was confirmed by flow cytometry analysis of oxidative stress induction [3].

To confirm whether ROS were implicated in the process of compound-induced cell cycle arrest and apoptosis, the level of intracellular ROS was analyzed. HepG2 cells were cultured for 24 h with compound **3** (1.5 and 3 μM), **5** (2 and 4 μM), **7** (1 and 2 μM), **9** (25 and 50 μM), **11** (25 and 50 μM), **13** (5 and 10 μM), **15** (10 and 20 μM), and **17** (7.5 and 15 μM) (Fig. 5, Fig. S44 (ESI)). The chosen concentration of each compound corresponds to a quarter and a half of the IC_{50} value. Compound **18** precipitated, thus impeding its correct oxidative stress assessment. Mitonafide and pinafide were tested as a reference compounds. The level of intracellular ROS generation was analyzed by dual staining with H_2DCFDA/PI. DCF green fluorescence is triggered in the presence of ROS proportional to oxidative stress intensity. The most potent ROS inducers were mitonafide and pinafide, whereas the naphthalimide-boron cluster conjugates were less effective, although the most promising were **3**, **15**, and **17** with approximately two times increase in fluorescence intensity; this finding showed that they were able to induce oxidative stress and generate ROS.

Studies performed so far have been shown that amongst all the modified conjugates, compound **17** is the most interesting one. Taking together its biological properties it shows almost the highest cytotoxicity towards HepG2 with IC_{50} = 29.10 μM activating cell death through apoptosis. Compound **17** also exert the greatest impact on cell cycle

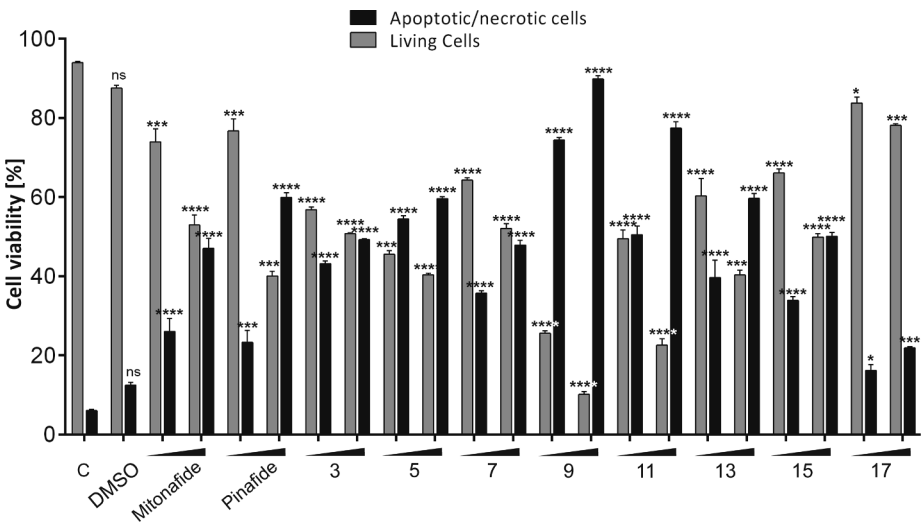

Fig. 3. Quantitative flow cytometry analysis of apoptosis in HepG2 cells after cell toxicity induction with compound **3** (3 and 6 μM), **5** (4 and 8 μM), **7** (2 and 4 μM), **9** (50 and 100 μM), **11** (50 and 100 μM), **13** (10 and 20 μM), **15** (20 and 40 μM), and **17** (15 and 30 μM). The cells were treated with increasing concentration of the tested compounds for 24 h. The chosen concentration of each compound corresponded to half of the IC_{50} or whole IC_{50} values. Level of apoptosis was evaluated with dual staining with YO-PRO-1/PI (live cells—gray bars, apoptotic/necrotic cells—black bars). Data are shown as mean ± SD. Statistical significance is indicated with asterisks: (*ns*) $p > 0.05$, (*) $p < 0.05$, (**) $p < 0.01$, (***) $p < 0.001$, (****) $p < 0.0001$.

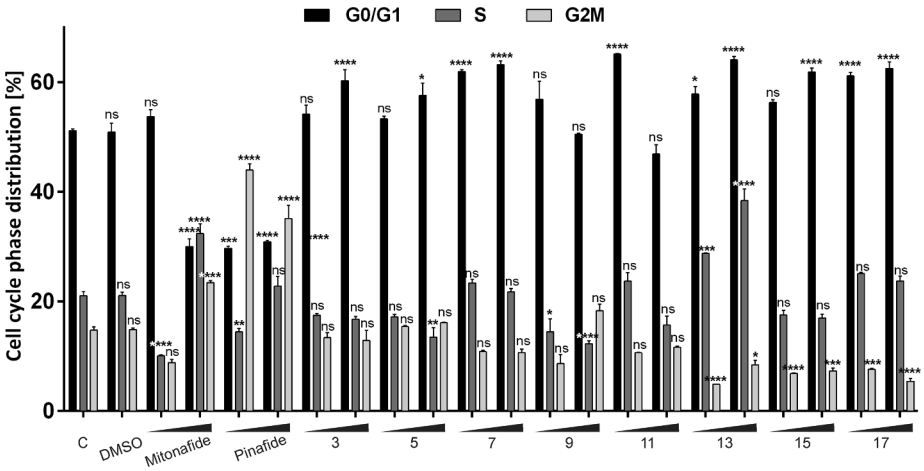

Fig. 4. Influence of compound **3** (3 and 6 μM), **5** (4 and 8 μM), **7** (2 and 4 μM), **9** (50 and 100 μM), **11** (50 and 10 μM), **13** (10 and 20 μM), **15** (20 and 40 μM), and **17** (15 and 30 μM) on cell cycle distribution in HepG2 cells. The cells were treated with increasing concentration of the tested compounds for 24 h. The chosen concentration of each compound corresponded to half of the IC_{50} and whole IC_{50} values. The graph shows percentage of cells in the G0/G1, S, and G2M stages. Cell cycle distribution was analyzed and presented as mean ± SD of three independent experiments. Statistical significance is indicated with asterisks: (*ns*) $p > 0.05$, (*) $p < 0.05$, (**) $p < 0.01$, (***) $p < 0.001$, (****) $p < 0.0001$.

resulting in G0/G1 arrest and induces intracellular ROS production. According to the data obtained so far, we chose compound **17** for further studies. The high ability of compound **17** to increase cellular ROS was confirmed by additional experiments. Confocal microscopy analysis help to present ROS activation by compound **17** in the cells. We observed increasing intracellular ROS in concentration dependent manner of compound **17**. This observation was confirmed together with flow cytometry analysis (Fig. 6).

2.2.5. Analysis of 8-oxo-dG in HepG2 cells

Among the various forms of DNA damage, oxidative DNA lesions caused by ROS that are generated both as a by-product of oxidative

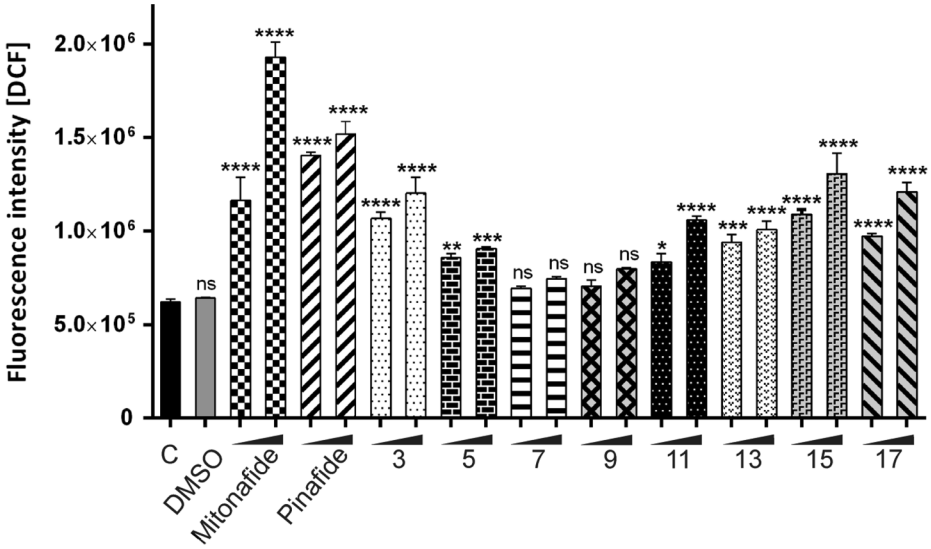

Fig. 5. ROS production in HepG2 cells after 24 h incubation with compound **3** (1.5 and 3 μM), **5** (2 and 4 μM), **7** (1 and 2 μM), **9** (25 and 50 μM), **11** (25 and 50 μM), **13** (5 and 10 μM), **15** (10 and 20 μM), and **17** (7.5 and 15 μM). The cells were treated with increasing concentration of the tested compounds. The chosen concentration of each compound corresponds to a quarter and a half of IC_{50} value. Intracellular production of ROS was measured by the dual H_2DCFDA/PI staining method. The intensity of DCF fluorescence corresponds to intracellular ROS level in HepG2 cells. Mean fluorescence intensity was measured by flow cytometry. Data are shown as mean ± SD of three independent experiments. Statistical significance is indicated with asterisks: (*ns*) $p > 0.05$, (*) $p < 0.05$, (**) $p < 0.01$, (***) $p < 0.001$, (****) $p < 0.0001$.

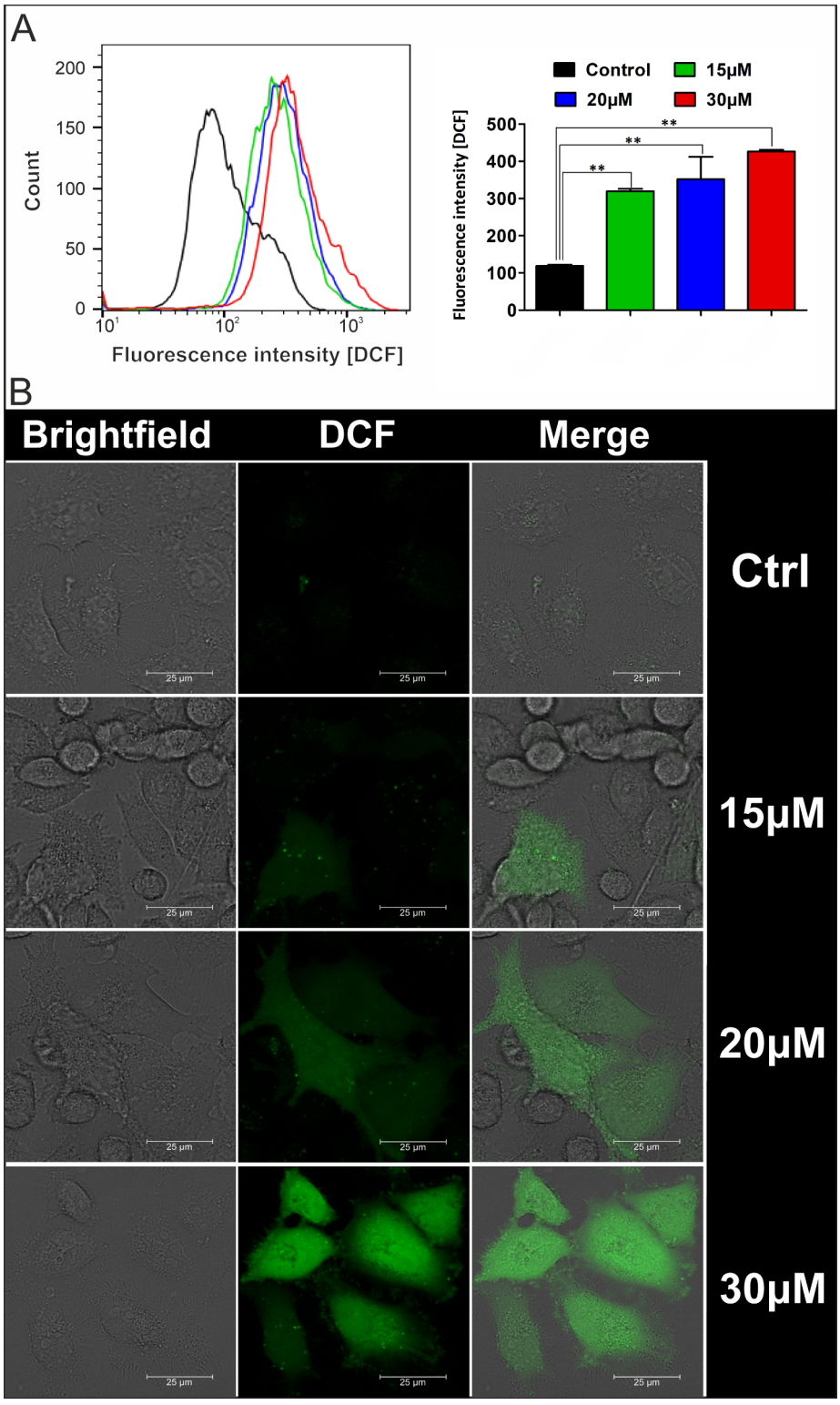

Fig. 6. Analysis of intracellular ROS production by H_2DCFDA staining. Flow cytometry analysis (A) of intracellular ROS in HepG2 cells treated with 15, 20 and 30 μM of compound **17** for 24 h, and confocal microscopy (B). Untreated cells were used as a control of experiment. Intensity of green signal is correlated with ROS level. A) The histogram of DCF fluorescence intensity from representative analysis by flow cytometry and the bar graph from the three independent experiments showed as a mean ± SEM. B) Left panels present images in bright-field, middle panels show HepG2 cell stained with H_2DCFDA, on the right panels merged images are presented. Scale bars, 25 μm. Statistical significance is indicated with asterisks: (*ns*) $p > 0.05$, (*) $p < 0.05$, (**) $p < 0.01$, (***) $p < 0.001$, (****) $p < 0.0001$.

metabolism and as a consequence of exposure to ionizing radiation and other environmental factors are considered to be a major threat to the genome [36,37]. Guanosine is known to be the most susceptible nucleotide to oxidation, and its oxidized form 8-oxo-dG is one of the major oxidation products in DNA [38]. When present in DNA, it causes a G:C to T:A transversion mutation during replication [39]. Under normal conditions, there is one 8-oxo-dG molecule per 10^5–10^6 guanosines in a genome, corresponding to thousands of 8-oxo-dG molecules per single cell. It can occur in DNA in two ways: direct oxidation of a guanine base in a genomic sequence or oxidation at the nucleotide pool levels, i.e., formation of 8-oxo-dGTP followed by its incorporation.

DNA methylation is a natural, covalent DNA modification process, which is common in eukaryotic cells. It involves the incorporation of a methyl group in the C-5 position of cytosine mainly in CpG dinucleotides, which leads to the formation of 5-methylcytidine (m^5dC). In a normal cell, m^5dC constitutes approximately 0.75–1% of all nucleotides in DNA and affects 70–80% of all CpG dinucleotides in the genome. Changes in DNA methylation patterns are related to vital processes such

Table 2
m^5dC and 8-oxo-dG level in cellular DNA after treatment with **17** and mitonafide.

Compound	$m^5dC/(dC + m^5dC) \pm SD$ [%]	8-oxo-dG/10^6dG ± SD
Control	4.25 ± 0.02	2.11 ± 0.08
17	4.14 ± 0.01	46.14 ± 0.05
Mitonafide	4.16 ± 0.06	28.24 ± 0.18

as aging, chronic inflammation, and cancer development [40].

By using HPLC-UV-ED, we determined the contents of 2′-deoxy-5-methylcytidine (m^5dC) and 2′-deoxy-8-oxoguanosine (8-oxo-dG) in enzymatic DNA hydrolysates from HepG2 cells treated with compound **17** (15 μM). Mitonafide (0.5 μM) was used as a positive control. The methylation of dC was calculated as follows: $m^5dC = m^5dC/(dC + m^5dC) \times 100\%$. The analyzed compound did not affect the level of m^5dC (epigenetic factor) compared to control cells (Table 2). The number of 8-oxo-dG was calculated per 10^6 dG. We showed that compound **17** significantly elevates the number of 8-oxo-dG molecules compared to untreated control. Moreover compound **17** treatment generates much higher oxidative disturbances in DNA than mitonafide, resulting in approximately two times more number of 8-oxo-dG (46.14 vs 28.24 per 10^6 dG, respectively). Our finding was additionally confirmed by immunofluorescence analysis of HepG2 cells after **17** treatment using anti-8-oxo-G/dG antibody (Fig. 7).

2.2.6. Mitochondrial oxidative stress induction in HepG2 cells by flow cytometry

One of the main sources of intracellular ROS is mitochondria, known as mitochondrial ROS (mtROS), which are produced in the form of superoxide anions (O_2^-) as a by-product of oxidative metabolism [35]. Mitochondrial production of ROS and the ensuing damage inflicted by these ROS on biological macromolecules, including DNA, constitutes the basis of the free radical/mitochondrial theory of aging. According to this theory, the production of ROS by mitochondria leads to mtDNA damage and mutations which in turn lead to progressive respiratory chain dysfunction and to a further increase in ROS production as a consequence of this dysfunction [41].

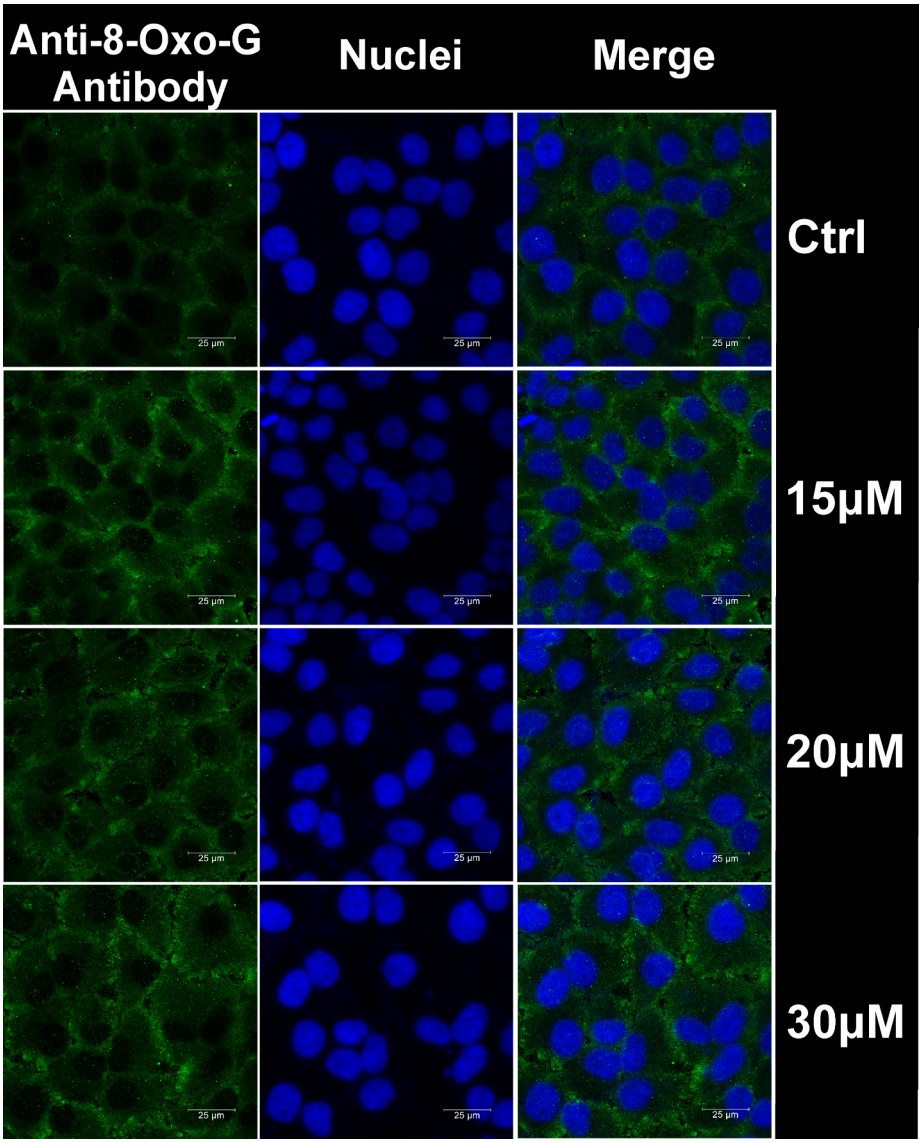

Fig. 7. Immunofluorescence analysis of intracellular 8-oxo-G/dG. Confocal microscopy analysis of 8-oxo-G/dG in HepG2 cells after 24 h treatment with compound **17** in the final concentration of 15, 20, and 30 μM. Untreated cells were used as a control of the experiment. The level of 8-oxoG/dG was detected by primary anti-8-G/dG-FITC antibody (green fluorescence, left panels), and the nuclei were stained with Hoechst 33,342 (blue fluorescence, middle panels). Intensity of green signal is correlated with the intracellular level of 8-oxoG/dG. Scale bars, 25 μm.

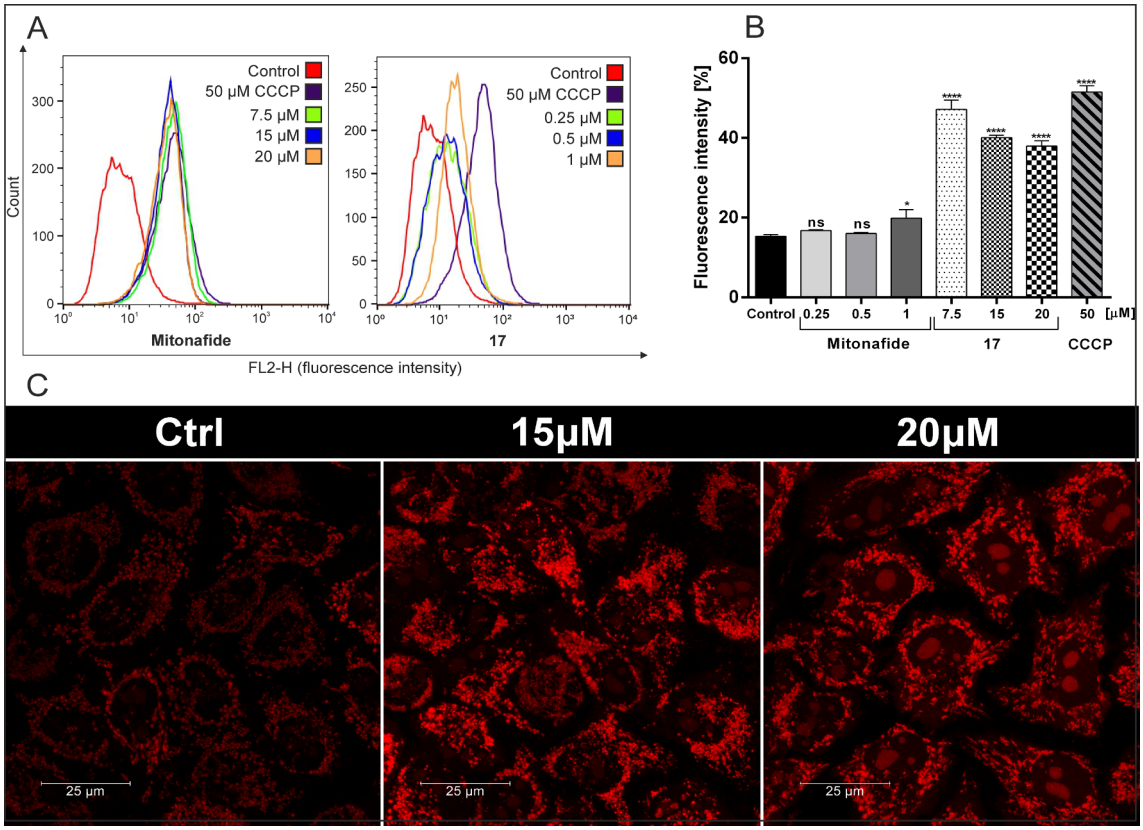

Fig. 8. Analysis of mitochondrial oxidative stress in HepG2 cells. Flow cytometry (A, B) and confocal microscopy (C) analysis of mitochondrial oxidative stress induction in HepG2 cells after mitonafide and **17** treatment. The cells were incubated with the compounds for 24 h and the mitochondrial oxidative stress was measured using mitochondrial fluorescent dye MitoSOX (3 μM), indicating superoxide level within the cells. Fluorescent signal was detected by FACSCalibur flow cytometer using 488 nm excitation laser. (A) Histograms of red fluorescence, where peak shift compared to control corresponds to the status of mitochondrial oxidation. To generate strong positive oxidation signal CCCP (50 μM) was used. (B) The data was plotted and presented as a mean ± SEM from three independent experiment. (C) Simultaneously mitochondrial oxidative status (for 7.5, 15 and 20 μM of compound **17**) was visualized by confocal microscope. Scale bars, 25 μm. Statistical significance is indicated with asterisks: (*ns*) $p > 0.05$, (*) $p < 0.05$, (**) $p < 0.01$, (***) $p < 0.001$, (****) $p < 0.0001$.

Table 3
ΔT_m of ct-DNA in the presence of **3**, **5**, **7**, **9**, **11**, **13**, **15**, **17**, **18**, and mitonafide.

Compound	ΔT_m [°C]
	ct-DNA
3	0
5	0.66
7	0.31
9	0
11	0.99
13	0.66
15	1.01
17	1.32
18	0.66
Mitonafide	8.00

Mitochondrial oxidative stress induction by mitonafide and compound **17** in HepG2 cells was analyzed by flow cytometry using MitoSOX staining. Red fluorescence of the dye is triggered selectively in mitochondria in the presence of superoxide (Fig. 8). Analysis after 24 h revealed that both analyzed compounds induce superoxide production in the cells, but at a different level. Mitonafide slightly induces superoxide production only at the highest concentration (1 μM) whereas compound **17** affects the cells significantly, with two times higher level of superoxide production. The observed decrease in fluorescence intensity in the cells treated with higher concentrations of compound **17** (15 and 20 μM) is most likely related to lower viability of the cells or might be due to the activation of antioxidant defense mechanism by cancer cells.

mtDNA is critical cellular target for ROS. Its lacks of histones that prevent ROS-induced DNA damage and thus less complex architecture in contrast to nuclear DNA. Exposure to ROS decreased mitochondrial function, increased mitochondrial-generated ROS and mitochondrial damage, consequently activating apoptosis much efficient than nuclear DNA damage.

2.3. Physicochemical investigation with DNA

DNA melting is the process of separating the double-helical DNA structure into two single strands from stable hydrogen bonding and base stacking interactions [42]. The melting temperature (T_m) of DNA is defined as the temperature at which half of the DNA strands are in the double-helical state and half in the random-coil state [43]. Helix melting of DNA is performed by measuring the absorbance at 260 nm as a function of temperature. A large increase in T_m (3–8 °C) is observed only for the strong intercalation type of interaction. In contrast, groove-binding interaction of small molecules with DNA leads to insignificant amendment of T_m. In this case, an experiment was carried out to monitor the change in T_m for calf thymus DNA (ct-DNA) in the absence and presence of modified naphthalimides to understand the interaction between them (Table 3 and Fig. S45 (ESI)).

Thermal melting experiments showed that the studied compounds **3**, **5**, **7**, **9**, **13**, and **18** showed negligible stabilization of ct-DNA. The only observed exception was that for conjugates **11**, **15**, and **17** modified with metallacarboranes, which caused better DNA stabilization, especially conjugate **17**. In comparison to mitonafide, conjugate **17**

rather excludes classical intercalation as a dominant binding mode, and indicates a different type of interaction with DNA.

In an effort to better understand the interactions of DNA and modified naphthalimides, circular dichroism measurements were conducted. Circular Dichroism (CD) is a powerful and reliable technique to investigate the conformational changes in DNA morphology during small molecule–DNA interactions. The CD spectra of the B-form of DNA duplex generally display a positive Cotton effect that appears at 270 nm and a negative effect at approximately 250 nm, with nearly equal magnitudes of longwave positive bands and shortwave negative bands [44,45]. Binding of a small, achiral molecule to a chiral DNA helix can result in the occurrence of an induced CD (ICD) signal of molecule.

The CD spectrum of free ct-DNA showed a negative band at 248 nm due to the polynucleotide helicity and a positive band at 276 nm due to the base stacking; this finding confirmed that the ct-DNA existed in the right-band B-form [46]. As illustrated in Fig. S46 (ESI), mitonafide led to a decrease of the negative peak and an increase of the positive peak. In contrast with mitonafide, compounds **3**, **5**, **7**, **9**, **11**, **13**, and **18** did not cause any appreciable change in the CD spectra of ct-DNA (Figs. S47–S51 (ESI)) with their increasing concentrations. Fig. S50 (ESI) shows the CD spectra of ct-DNA in the absence and presence of **15** and **17**. The positive and negative bands were perturbed by the presence of both tested compounds. These observations seem to indicate that **15** and **17** interact stronger with DNA than other tested naphthalimides bearing boron cluster but weaker than mitonafide. It should be noted that **15** and **17** are chiral. This may be possible because only one enantiomer is intercalated. Relatively little is known for interactions between chiral intercalators with DNAs [47], especially naphthalimides. Several novel heterocyclic-fused naphthalimide intercalators with chiral amino side chain exhibited different DNA-binding activities, DNA-photodamaging activities, and antitumor cytotoxicity depending on whether they were S-or R-enantiomer [48].

3. Conclusions

In summary, we have elaborated convenient protocols for the synthesis of new naphthalimides modified with boron cluster-carborane (*ortho*-, *meta*-, and *para*-) or metallacarborane (cobalt/chromium bis (1,2-dicarbollide) (1–) anion) group, as analogs of mitonafide. The X-ray structure of the naphthalimide-carborane conjugates **5** and **7** was established, thus providing the first example of X-ray analysis of naphthalimide-boron cluster conjugate. Cytotoxic properties of compounds **3**, **5**, **7**, **9**, **11**, **13**, **15**, **17** were studied on human cancer cell lines: HepG2 and RPMI 2650. It was found that the type of boron group affected various cytotoxic activities of the tested compounds. Naphthalimides containing carborane cluster were more cytotoxic than those containing metallacarborane against both cell lines. More importantly, flow cytometric analysis indicated that naphthalimide-boron cluster conjugate could effectively induce G0/G1 arrest and promote mainly apoptosis in HepG2 cell line after double staining with YO-PRO-1 and propidium iodide. We selected compound **17** as the most promising among the synthesized ones. It is a potent mitochondrial ROS inducer what underlies its mechanism of action. ROS exposure contributes to mitochondrial dysfunction leading to cellular stress response, growth arrest and consequently apoptosis.

Additionally to biological assays the interaction of the new compounds with ct-DNA was studied by CD spectra and melting temperature, thus demonstrating that these compounds were rather weak classical DNA intercalators, in comparison to mitonafide, that indicates another type of interaction with DNA.

The present work demonstrated that incorporating the biological active unit of naphthalimide and inorganic boron cluster might be able to result in a novel class of lead compounds with potential antitumor activities. Studies on the development of new analogs of mitonafide and pinafide containing boron clusters in a different position of the naphthalic ring are currently in progress in our laboratory.

4. Experimental

4.1. Chemistry

4.1.1. Materials and methods

Most of the chemicals were obtained from the Acros Organics (Geel, Belgium) and were used without further purification unless otherwise stated. Boron clusters were purchased from KATCHEM spol. s.r.o. (Řež/Prague, Czech Republic). All experiments that involved water-sensitive compounds were conducted under rigorously dry conditions and under an argon atmosphere. Flash column chromatography was performed on silica gel 60 (230–400 mesh, Sigma-Aldrich). R_f refer to analytical TLC performed using pre-coated silica gel 60 F254 plates purchased from Sigma-Aldrich (Steinheim, Germany) and developed in the solvent system indicated. Compounds were visualized by use of UV light (254 nm) or a 0.5% acidic solution of $PdCl_2$ in HCl/methanol by heating with a heat gun for boron-containing derivatives. The yields are not optimized.

^{1}H, ^{11}B and ^{13}C NMR spectroscopy for compound **3**, **5**, **7** was performed on a Bruker Ultra Shield 700 MHz spectrometer. The spectra for ^{1}H, ^{13}C, and ^{11}B were recorded at 699.73 MHz, 175.95 MHz, and 244.50 MHz, respectively. Deuterated acetone was used as standard.

^{1}H, ^{11}B and ^{13}C NMR spectroscopy for compound **9** was performed on a JEOL ECZ 600R. ^{1}H (600.17 MHz) and ^{13}C NMR (150.91 MHz) chemical shifts are referred to the residual ^{1}H signal of a deuterated acetone. ^{11}B NMR (192.56 MHz) chemical shifts are given in ppm to high-frequency (low field) to $F_3B{\cdot}OEt_2$ as the external reference.

^{1}H, ^{11}B and ^{13}C NMR spectroscopy for compounds **11**, **13**, **17**, **18** was performed on a Varian Mercury 400^{Plus} Instrument. ^{1}H (399.98 MHz) and ^{13}C NMR (100.59 MHz) chemical shifts are referred to the residual ^{1}H signal(s) of a deuterated acetone. δ ($^{1}H\{^{11}B\}$) data are presented and their assignment is based on selectively decoupled $\delta(^{1}H)$-$\{^{11}B$ selective$\}$NMR experiments. ^{11}B NMR (128.33 MHz) chemical shifts are given in ppm to high-frequency (low field) to $F_3B{\cdot}OEt_2$ as the external reference. Coupling constants $^{1}J(^{11}B–^{1}H)$ were measured by resolution-enhanced ^{11}B spectra with a digital resolution of 2 Hz and are given in Hz. The following abbreviations are used to denote the multiplicities: s = singlet, d = doublet, dd = doublet of doublets, ddd = doublet of doublets of doublets, t = triplet, dt = doublet of triplets, q = quartet, quin = quintet, bs = broad singlet, and m = multiplet. *J* values are given in Hz.

Mass spectra for compounds **3**, **5**, **7** were recorded on a CombiFlash PurIon Model Eurus35 (Teledyne ISCO, Lincoln, USA). The ionization was achieved by electrospray ionization in the positive ion mode (ESI +) and negative ion mode (ESI−). The capillary voltage was set to 2.5 kV. The source temperature was 350 °C, and the cone temperature was 300 °C. Nitrogen was used as a desolvation gas (flow 35 L/min, purity > 99%).

Mass spectra for compounds **9**, **11**, **13**, **15**, **17**, **18** were performed on a Thermo Finnigan LCQ-Fleet Ion Trap instrument using electrospray (ESI) ionization. Negative ions were detected. Samples dissolved in acetonitrile (concentrations approx. 100 ng mL^{-1}) were introduced to the ion source by the infusion of 5 μL min^{-1}, source voltage-5.57 kV, tube lens voltage-49.8 V, capillary voltage-10.0 V, drying temperature at 188 °C, drying gas flow 8 L min^{-1} and auxiliary gas pressure 6 Bar. The data are presented for the most abundant mass in the boron distribution plot of the base peak (100%) and for the peak corresponding to the highest *m/z* value with its relative abundance (%).

The theoretical molecular mass peaks of the compounds were calculated using the “Show Analysis Window” option in the ChemDraw Ultra 12.0 program. The calculated *m/z* corresponds to the average mass of the compounds consisting of natural isotopes.

Infrared absorption spectra (IR) were recorded using a Nicolet 6700 Fourier-transform infrared spectrometer from Thermo Scientific equipped with a ETC EverGlo* source for the IR range, a Ge-on-KBr beam splitter, and a DLaTGS/KBr detector with a smart orbit sampling

compartment and diamond window. The samples were placed directly on the diamond crystal, and pressure was added to make the surface of the sample conform to the surface of the diamond crystal.

UV measurements were performed using a GBC Cintra10 UV–VIS spectrometer (Dandenong, Australia). The samples used for the UV experiment were dissolved in 95% C_2H_5OH. The measurement was performed at ambient temperature.

Crystals of **5** and **7** were obtained by slow evaporation from ethanol. The X-ray diffraction measurements were performed at the BESSY synchrotron, Berlin, on beam line MX 14.3, on Rayonix MX225 detector at the X-ray wavelength of 0.89429 Å, on crystals cooled to 100 K in a stream of cold nitrogen gas. X-ray data were collected on each crystal to the resolution of 0.8 Å and the data were processed using the HKL200 program suite [49]. The structures were solved with SHELXT [50] and refined with SHELXL program suite [51].

1-(3-Aminopropyl)-1,2-dicarba-closo-dodecaborane hydrochloride, 1,2-$C_2B_{10}H_{11}$-$(CH_2)_3NH_2HCl$ ***(2)*** was synthesized as described in the literature [23]. *1-(3-Aminopropyl)-1,7-dicarba-closo-dodecaborane hydrochloride, 1,7-$C_2B_{10}H_{11}$-$(CH_2)_3NH_2HCl$* ***(4)*** was synthesized as described in the literature [26]. *1-(3-aminopropyl)-1,12-dicarba-closo-dodecaborane hydrochloride, 1,12-$C_2B_{10}H_{11}$-$(CH_2)_3NH_2HCl$* ***(6)*** were synthesized using the same method that was previously reported for the preparation of the corresponding 1-(3-aminopropyl)-1,2-dicarba-*closo*-dodecaborane hydrochloride (**2**) [23].

The synthesis of **4** and **6** was initiated by reacting *closo*-1,7-carborane/*closo*-1,12-carborane with butyl lithium in anhydrous THF at −78 °C without protection of one carbon atom with *tert*-butyldimethylsilyl group. diBoc groups, during synthesis of compound **4**, were removed using HCl/ether instead of TFA/CH_2Cl_2.

8-(5-Ammonio-3-oxa-pentoxy)-3,3′-commo-bis(1,2-dicarba-3-cobalt (III)-closo-dodecabor)ate (–1), [8-(5-NH_3-$(OCH_2CH_2)_2$-3,3′-Co(1,2-$C_2B_9H_{10}$)(1′,2′-$C_2B_9H_{11}$)]$^-$ ***(8)*** was synthesized as described in the recent literature [24]. *8-(5-Ammonio-3-oxa-pentoxy)-3,3′-commo-bis(1,2-dicarba-3-chromium(III)-closo-dodecabor)ate (–1), [8-(5-NH_3-$(OCH_2CH_2)_2$-3,3′-Cr(1,2-$C_2B_9H_{10}$)(1′,2′-$C_2B_9H_{11}$)]$^-$* ***(10)*** was obtained in analogy, starting from known *8-(dioxane)-3,3′-commo-bis(1,2-dicarba-3-chromium(III)-closo-dodecabor)ate z*witterion [27] and using the same procedure as for **8**.

1-Aminopropyl-3,3′-commo-bis(1,2-dicarba-3-cobalt(III)-closo-dodecaborane) tetramethyl ammonium salt, [(1-NH_2-$(CH_2)_3$-3,3′-Co(1,2-$C_2B_9H_{10}$)(1′,2′-$C_2B_9H_{11}$)]Me_4N ***(12)****, 1-aminoethyl-3,3′-commo-bis(1,2-dicarba-3-cobalt(III)-closo-dodecaborane) tetramethyl ammonium salt, [(1-NH_2-$(CH_2)_2$-3,3′-Co(1,2-$C_2B_9H_{10}$)(1′,2′-$C_2B_9H_{11}$)]Me_4N* ***(14)****, 1,1′-di (aminoethyl)-3,3′-commo-bis(1,2-dicarba-3-cobalt(III)-closo-dodecaborane) tetramethyl ammonium salt, [(1,1′-(NH_2-$(CH_2)_2$-3,3′-Co(1,2-$C_2B_9H_{10}$)(1′,2′-$C_2B_9H_{10}$)]Me_4N* ***(16)*** were synthesized as described previously [25].

*4.1.2. General synthesis of naphthalimide derivatives **3**, **5**, **7** modified with carborane cluster*

A suspension of 3-nitro-naphthalic anhydride (**1**) (1 eq.) in absolute EtOH (0.5 mL per 0.1 mmol) was treated with TEA (2 eq.) and solution of appropriate amine **2**, **4** or **6** (1 eq.) in absolute EtOH (0.25 mL per 0.1 mmol) dropwise was added. The reaction mixture was stirred for 6 h in 65 °C under an inert (Ar) atmosphere. Subsequently, the solvents were evaporated to dryness under vacuum and purified by silica gel column chromatography using a gradient elution from 0 to 10% hexane in CH_2Cl_2.

N-[3-(1,2-dicarba-closo-dodecaborane-1-yl)propyl]-1,8-naphthalimide ***(3)***: yellowish solid, yield 28.19 mg (64%). TLC (hexane:CH_2Cl_2, 1:9 v/v): R_f = 0.23; ^{1}H NMR (acetone-d_6, 699.73 MHz): δ (ppm) = 9.33 (1H, d, J = 2.10 Hz, H-4), 9.06 (1H, d, J = 2.8 Hz, H-7), 8.73–8.71 (2H, m, H-5, H-2), 8.06 (1H, dd, H-6), 4.68 (1H, br s, CH-carborane), 4.15 (2H, t, J = 6.99 Hz, N$CH_2CH_2CH_2$), 2.58–2.55 (2H, m, $NCH_2CH_2CH_2$), 2.50–1.75 (10*H*, br m, B-H), 2.03–1.99 (2H, m, $NCH_2CH_2CH_2$); ^{13}C NMR (acetone-d_6, 175.95 MHz): δ (ppm) = 164.00 (1C, C═O), 163.51 (1C, C═O), 147.32 (1C, C-3), 137.00 (1C, C-4), 134.89 (1C, C-7), 132.26 (1C, C-5), 131.02 (1C, C-6), 130.25 (1C, C-2), 130.16 (1C, C-10), 125.65 (1C, C-1), 124.20 (1C, C-9), 124.05 (1C, C-8), 76.95 (1C, C-carborane), 63.60 (1C, CH-carborane), 40.33 (1C, N$CH_2CH_2CH_2$), 35.96 (1C, $NCH_2CH_2CH_2$), 28.81 (1C, $NCH_2CH_2CH_2$); ^{11}B NMR (acetone-d_6, 224.50 MHz): δ (ppm) = –2.92 (1B, d, J = 145 Hz, B-9), –6.08 (1B, d, J = 138 Hz, B-12), –9.65 (2B, d, J = 152 Hz, B-8, B-10), –11.46 (2B, d, J = 153 Hz, B-4, B-5), –11.94 (2B, d, J = 132 Hz, B-3, B-6), –13.07 (2B, d, J = 174 Hz, B-7, B-11); UV (95% C_2H_5OH): λ_{min} (nm) = 237, 307, λ_{max} = 274, 332, λ_{sh} = 320, 347, 362; FT-IR: ν_{max} (cm^{-1}) = 3064 (CH arom), 2964, 2922, 2851 (CH alkyl), 2583 (BH), 1704, 1659 (C═O), 1594, 1332 (NO_2), 1538, 1508, 1455, 1420 (C═C), 721 (BB); ESI-MS: *m/z*: 426 (100%), calcd for $C_{17}H_{22}B_{10}N_2O_4$: 426.26.

N-[3-(1,7-dicarba-closo-dodecaborane-1-yl)propyl]-1,8-naphthalimide ***(5)***: yellowish solid, yield 32.03 mg (73%). TLC (hexane:CH_2Cl_2, 1:9 v/v): R_f = 0.28; ^{1}H NMR (acetone-d_6, 699.73 MHz): δ (ppm) = 9.30 (1H, d, J = 2.10, H-4), 9.04 (1H, d, J = 2.10, H-7), 8.70–8.69 (2H, m, H-5, H-2), 8.05 (1H, t, J = 7.70 Hz, H-6), 4.09 (2H, t, J = 7.70 Hz, N$CH_2CH_2CH_2$), 3.63 (1H, br s, CH-carborane), 3.00–1.50 (10*H*, br m, B-H), 2.21 (2H, t, J = 8.40 Hz, $NCH_2CH_2CH_2$), 1.90–1.85 (2H, m, $NCH_2CH_2CH_2$); ^{13}C NMR (acetone-d_6, 175.95 MHz): δ (ppm) = 163.89 (1C, C═O), 163.40 (1C, C═O), 147.28 (1C, C-3), 136.92 (1C, C-4), 134.83 (1C, C-7), 132.22 (1C, C-5), 130.97 (1C, C-6), 130.17 (1C, C-2), 130.12 (1C, C-10), 125.64 (1C, C-1), 124.18 (1C, C-9), 124.00 (1C, C-8), 77.31 (1C, C-carborane), 56.80 (1C, CH-carborane), 40.55 (1C, N$CH_2CH_2CH_2$), 35.17 (1C, $NCH_2CH_2CH_2$), signal from $NCH_2CH_2CH_2$ overlaped with signal from acetone; ^{11}B NMR (acetone-d_6, 224.50 MHz): δ (ppm) = –4.31 (1B, d, J = 158 Hz, B-5), –9.98 (1B, m, Hz, B-12), –11.00 (4B, d, J = 154 Hz, B-9, B-10, B-4, B-6), –13.56 (2B, d, J = 161 Hz, B-8, B-11), –15.07 (2B, d, J = 180 Hz, B-2, B-3); UV (95% C_2H_5OH): λ_{min} (nm) = 238, 307, λ_{max} = 275, 332, λ_{sh} = 318, 348, 362; FT-IR: ν_{max} (cm^{-1}) = 3074 (CH arom), 2959, 2924, 2852 (CH alkyl), 2595 (BH), 1706, 1662 (C═O), 1598, 1328 (NO_2), 1536, 1507, 1435, 1420 (C═C), 729 (BB); ESI-MS: *m/z*: 426 (100%), calcd for $C_{17}H_{22}B_{10}N_2O_4$: 426.26.

N-[3-(1,12-dicarba-closo-dodecaborane-1-yl)propyl]-1,8-naphthalimide ***(7)***: yellowish solid, yield 33.06 mg (75%). TLC (hexane:CH_2Cl_2, 1:9 v/v): R_f = 0.22; ^{1}H NMR (acetone-d_6, 699.73 MHz): δ (ppm) = 9.29 (1H, d, J = 2.10, H-4), 9.02 (1H, d, J = 2.10, H-7), 8.69–8.66 (2H, m, H-5, H-2), 8.03 (1H, t, J = 7.7 Hz, H-6), 3.97 (2H, t, J = 7.70 Hz, N$CH_2CH_2CH_2$), 3.26 (1H, br s, CH-carborane), 2.70–1.50 (10*H*, br m, B-H), 1.86 (2H, t, J = 7.70 Hz, $NCH_2CH_2CH_2$), 1.67–1.62 (2H, m, $NCH_2CH_2CH_2$); ^{13}C NMR (acetone-d_6, 175.95 MHz): δ (ppm) = 163.81 (1C, C═O), 163.32 (1C, C═O), 147.27 (1C, C-3), 136.90 (1C, C-4), 134.82 (1C, C-7), 132.20 (1C, C-5), 130.94 (1C, C-6), 130.15 (1C, C-2), 130.11 (1C, C-10), 125.61 (1C, C-1), 124.14 (1C, C-9), 123.99 (1C, C-8), 85.18 (1C, C-carborane), 59.79 (1C, CH-carborane), 40.49 (1C, N$CH_2CH_2CH_2$), 37.11 (1C, $NCH_2CH_2CH_2$), 28.74 (1C, $NCH_2CH_2CH_2$); ^{11}B NMR (acetone-d_6, 224.50 MHz): δ (ppm) = –12.61 (5B, d, J = 158 Hz), –15.07 (5B, d, J = 154 Hz); UV (95% C_2H_5OH): λ_{min} (nm) = 237, 306, λ_{max} = 274, 331, λ_{sh} = 320, 348, 362; FT-IR: ν_{max} (cm^{-1}) = 3073 (CH arom), 2958, 2926, 2853 (CH alkyl), 2600 (BH), 1707, 1662 (C═O), 1598, 1328 (NO_2), 1537, 1507, 1436, 1419 (C═C), 728 (BB); ESI-MS: *m/z*: 426 (100%), calcd for $C_{17}H_{22}B_{10}N_2O_4$: 426.26.

*4.1.3. General synthesis of naphthalimide derivatives **9**, **11**, **13**, **15** modified with metallacarborane group*

A suspension of 3-nitro-1,8-naphthalic anhydride (**1**) (1 eq.) in absolute EtOH (20 mL per 0.1 mmol) was treated with TEA (2 eq.) and solution of appropriate amine **8**, **10**, **12** or **14** (1 eq.) in absolute EtOH (10 mL per 0.1 mmol) dropwise was added. The reaction mixture was stirred for 5 h at 60 °C under an inert (Ar) atmosphere. Subsequently, the solvents were evaporated to dryness under vacuum and purified by silica gel column chromatography using a gradient elution from 0 to 20% CH_3CN in CH_2Cl_2.

*N-[(8-(3-oxa-pentoxy)-3,3′-commo-bis(1,2-dicarba-3-cobalta(III)-closo-dodecaborate)]-1,8-naphthalimide (**9**)*: yellow solid, yield 7.5 mg (yield 58%). TLC (CH_2Cl_2:CH_3CN 4:1, v/v): R_f = 0.50; ^{1}H NMR (acetone-d_6, 600.17 MHz): δ (ppm) = 9.28 (1H, d, J = 1.8 Hz, H-4), 9.03 (1H, d, J = 2.4 Hz, H-7), 8.67 (1H, d, J = 1.8 Hz, H-5), 8.66 (1H, s, H-2), 8.02 (1H, t, J = 8.4 Hz, H-6), 4.36 (2H, t, J = 6.6 Hz, OCH_2CH_2N), 4.14 (2H, br s, CH_2-carborane), 4.12 (2H, br s, CH_2-carborane), 4.36 (2H, t, $J_{1,2}$ = 6.6, $J_{1,3}$ = 12.6 Hz, O-CH_2CH_2N), 3.57 (4H, m, $BOCH_2CH_2OCH_2CH_2N$); ^{13}C NMR (acetone-d_6, 150.91 MHz): δ (ppm) = 163.11 (1C, C═O), 162.69 (1C, C═O), 146.36 (1C, C-3), 136.13 (1C, C-4), 134.15 (1C, C-7), 131.33 (1C, C-5), 130.21 (1C, C-6), 129.38 (1C, C-2), 129.24 (1C, C-10), 124.59 (1C, C-1), 123.34 (1C, C-9), 123.10 (1C, C-8), 71.77 (1C, CH_2CH_2N), 68.51 (1C, OCH_2CH_2N), 67.82 (1C, OCH_2CH_2O), 54.03 (1C, CH-carborane), 46.52 (1C, CH-carborane), 39.63 (1C, OCH_2CH_2OB); ^{11}B NMR (acetone-d_6, 192.56 MHz): δ (ppm) = 22.17 (1B, s, B-8), 3.28 (1B, d, J = 128 Hz, B-8́), –0.63 (1B, d, J = 136 Hz, B-10́), − 3.43 (1B, d, J = 138 Hz, B-10), –5.44 (2B, d, J = 134 Hz B-9, 9́), –8.31 (2B, d, J = 141 Hz B-12, 12́), –9.04 (4B, d, J = 127 Hz B-4, 4́, 7, 7́), –18.30 (2B, d, J = 155 Hz, B-5, 5́), –21.47 (2B, d, J = 150 Hz, B-11, 11́), –23.06 (1B, d, *overlap*, B-6), –29.52 (1B, d, J = 143 Hz, B-6́); UV (95% C_2H_5OH): λ_{min} (nm) = 238, 295, λmax = 276, 314; FT-IR: ν_{max} (cm^{-1}) = 3648–3545 (CH arom), 3077, 3044, 2923, 2879 (CH alkyl), 2535 (BH), 1705, 1660 (C═O), 1599, 1331 (NO_2), 1540, 1508, 1435, 1422 (C═C); ESI-MS: *m/z*: 651.50 (80%), 652.50 (100%), calcd for $C_{20}H_{34}B_{18}CoN_2O_6$: 651.36.

*N-[(8-(3-oxa-pentoxy)-3,3′-commo-bis(1,2-dicarba-3-chromium(III)-closo-dodecaborate)-]-1,8-naphthalimide (**11**):* brown solid, 48.7 mg (yield 45%). TLC (CH_2Cl_2:CH_3CN 4:1, v/v): R_f = 0.45; Cr^{3+} is a paramagnetic nucleus that causes very broad span of the spectra (over 2000 ppm for ^{11}B NMR). Furthermore, the signals for B(8, 4, 7) and C(1, 2) atoms sitting in the carborane ligand face bonded to Cr(III) atom are so broadened that their position could not be reliably identified. Therefore the NMR spectra seems not a reliable tool for characterization of this particular kind of paramagnetic compounds and chemical shifts are thus not listed here; UV (95% C_2H_5OH): λ_{min} (nm) = 231, 254, 294, λ_{max} = 240, 267, 313; FT-IR: ν_{max} (cm^{-1}) = 3648–3522 (CH arom), 2956, 2922, 2861, 22,852 (CH alkyl), 2532 (BH), 1705, 1661 (C═O), 1600, 1333 (NO_2), 1541, 1508, 1456, 1423 (C═C); ESI-MS: *m/z*: 644.67 (90%), 645.67 (100%), calcd for $C_{20}H_{34}B_{18}CrN_2O_6$: 644.36.

*N-[3-(3,3′-commo-bis(1,2-dicarba-3-cobalta(III)-closo-dodecaborate-1-yl)propyl)]-1,8-naphthalimide (**13**)*: orange solid, yield 36.3 mg (37%). TLC (CH_2Cl_2:CH_3CN 4:1, v/v): R_f = 0.43; ^{1}H NMR (acetone-d_6, 399.98 MHz): δ (ppm) = 9.33 (1H, d, J = 4.0 Hz, H-4), 9.06 (1H, d, J = 2.4 Hz, H-7), 8.72 (1H, s, H-2), 8.71 (1H, t, J = 3.6 Hz, H-5), 8.08 (1H, t, J = 7.6 Hz, H-6), 4.15 (2H, t, J = 6.8 Hz, $CCH_2CH_2CH_2N$), 4.04 (1H, br s, CH-carborane), 3.68 (1H, br s, CH-carborane), 3.58 (1H, br s, CH-carborane), 3.54 (2H, q, $J_{1,2}$ = 7.6, $J_{1,3}$ = 14.8 Hz, $CCH_2CH_2CH_2N$), 2.89 (1H, m, $CCH_2CH_2CH_2N$), 2.53 (1H, m, $CCH_2CH_2CH_2N$); ^{13}C NMR (acetone-d_6, 100.59 MHz): δ (ppm) = 163.90 (1C, C═O), 163.40 (1C, C═O), 147.09 (1C, C-3), 136.80 (1C, C-4), 134.83 (C-7), 132.07 (1C, C-5), 130.91 (1C, C-6), 130.08 (1C, C-2), 129.97 (1C, C-10), 125.56 (1C, C-1), 124.06 (1C, C-9), 123.84 (1C, C-8), 69.48 (1C, C-carborane), 57.94 (1C, $CCH_2CH_2CH_2N$), 53.92 (1C, CH-carborane), 51.81 (1C, CH-carborane), 48.16 (1C, $CCH_2CH_2CH_2N$), 40.85 (1C, $CCH_2CH_2CH_2N$), 38.35 (1C, CH-carborane); ^{11}B NMR (acetone-d_6, 128.33 MHz): δ (ppm) = 6.61 (2B, d, J = 125 Hz, B-8, 8́), 0.83 (2B, d, J = 143 Hz, B-10, 10́), –5.98 (8B, d, J = 137 Hz, B-4, 4́, 7, 7́, 9, 9́, 12, 12́), –15.16 (1B, d, *overlap*, B-5), –16.44 (1B, d, *overlap*, B-5́), –17.80 (2B, d, J = 171 Hz, B-11, 11́), –19.47 (1B, d, *overlap*, B6), –23.05 (1B, d, J = 143 Hz, B-6́); UV (95% C_2H_5OH): λ_{min} (nm) = 238, λ_{max} = 276; FT-IR: ν_{max} (cm^{-1}) = 3631–3590 (CH arom), 2920, 2850 (CH alkyl), 2533 (BH), 1701, 1699 (C═O), 1599, 1330 (NO_2), 1539, 1507, 1436, 1422 (C═C); ESI-MS: *m/z*: 605.58 (90%), 606.50 (100%), calcd for $C_{19}H_{32}B_{18}CoN_2O_4$: 605.35.

*N-[2-(3,3′-commo-bis(1,2-dicarba-3-cobalta(III)-closo-dodecaborate-1-yl)ethyl)]-1,8-naphthalimide (**15**)*: orange solid, yield 74.5 mg (57%). TLC (CH_2Cl_2:CH_3CN 4:1, v/v): R_f = 0.50; ^{1}H NMR (acetone-d_6, 399.98 MHz): δ = 9.38 (1H, d, J = 2.0 Hz, H-4), 9.12 (1H, d, J = 2.4 Hz, H-7), 8.77 (2H, t, J = 8.4 Hz, H-2, H-5), 8.11 (1H, t, J = 8.4, H-6), 4.41 (2H, m, CCH_2CH_2N), 4.30 (2H, m, CCH_2CH_2N), 4.14 (1H, br s, CH-carborane), 3.82 (1H, br s, CH-carborane), 3.70 (1H, br s, CH-carborane); ^{13}C NMR (acetone-d_6, 100.59 MHz): δ = 136.82 (1C, C-3), 134.71 (1C, C-4), 132.16 (1C, C-7), 130.92 (1C, C-5), 130.11 (1C, C-6), 130.02 (1C, C-2), 126.14 (1C, C-10), 125.67 (1C, C-1), 124.21 (1C, C-9), 123.90 (1C, C-8), 66.38 (1C, C-carborane), 57.37 (1C, CCH_2CH_2N), 54.20 (1C, CH-carborane), 51.93 (1C, CH-carborane), 48.08 (1C, CH-carborane), 41.83 (1C, CCH_2CH_2N); ^{11}B NMR (acetone-d_6, 128.33 MHz): δ = 6.79 (2B, d, J = 131 Hz, B-8, 8́), 0.86 (2B, d, J = 140 Hz, B-10, 10́), –6.04 (8B, d, J = 119 Hz, B-4, 4́, 7, 7́, 9, 9́, 12, 12́), –16.25 (1B, d, J = 143 Hz, B-5), –17.72 (3B, d, J = 162 Hz, B-5́, 11, 11́), –19.69 (1B, d, *overlap*, B6), –22.92 (1B, d, J = 186 Hz, B-6́); UV (95% C_2H_5OH): λ_{min} (nm) = 237, λ_{max} = 284; FT-IR: ν_{max} (cm^{-1}) = 3650–3500 (CH arom), 2921, 2851 (CH alkyl), 2530 (BH), 1703, 1660 (C═O), 1598, 1331 (NO_2), 1540, 1508, 1455, 1402 (C═C); ESI-MS: *m/z*: 591.58 (80%), 592.50 (100%), calcd for $C_{18}H_{30}B_{18}CoN_2O_4$: 593.33.

*4.1.4. Synthesis of naphthalimide derivatives **17** and **18** modified with metallacarborane group*

A suspension of 3-nitro-1,8-naphthalic anhydride (**1**) (177 mg, 0.73 mmol) in absolute EtOH (10 mL) was treated with TEA (0.13 mL, 0.97 mmol) and solution of [1,1́-(NH_3-$(CH_2)_2$–1,2-$C_2B_9H_{10})_2$–3,3́-Co]$^+$ (**16**) (100 mg, 0.24 mmol) in absolute EtOH (5 mL) dropwise was added. The reaction mixture was stirred for 5 h at 60 °C under an inert (Ar) atmosphere. Subsequently, the solvents were evaporated to dryness under vacuum, and the crude products were purified by silica gel column chromatography using a gradient elution from 0 (to remove organic side products) to 20% CH_3CN in CH_2Cl_2, The separation of product **17** and **18** was carried out on the silica gel using a gradient elution from 0 to 12% CH_3CN in CH_2Cl_2.

*N-{[2-(3,3′-commo-bis(1,2-dicarba-3-cobalta(III)-closo-dodecaborate-1-yl)ethyl]-1′-aminoethyl)}-1,8-naphthalimide] (**17**)*: red solid, yield 10.3 mg (7%). TLC (CH_2Cl_2:CH_3CN 7:1, v/v): R_f = 0.41; ^{1}H NMR (acetone-d_6, 399.98 MHz): δ = 9.37 (1H, s, H-2), 9.10 (1H, d, J = 5.2 Hz, H-4), 8.74 (2H, t, J = 11.2 Hz, H-5, H-7), 8.10 (1H, t, J = 7.6, H-6), 5.63 (2H, s, NH_2), 4.40 (2H, t, J = 7.6 Hz, CCH_2CH_2N), 4.02 (1H, br s, CH-carborane), 3.85 (1H, br s, CH-carborane), 3.74 (2H, t, J = 10.8 Hz, $CCH_2CH_2NH_2$), 3.54 (2H, m, CCH_2CH_2N), 2.90 (2H, m, $CCH_2CH_2NH_2$); ^{13}C NMR (acetone-d_6, 100.59 MHz): δ = 163.47 (1C, C═O), 163.07 (1C, C═O), 147.21 (1C, C-3), (1C, C-4), 136.79 (1C, C-7), 134.73 (1C, C-5), 130.91 (1C, C-2), 130.06 (2C, C-6, C-10), 125.60 (1C, C-1), 124.19 (1C, C-9), 123.90 (1C, C-8), 62.63 (1C, C-carborane), 59.99 (1C, CCH_2CH_2N), 58.90 (1C, CH-carborane), 58.82 (1C, CH-carborane), 57.56 (1C, CH-carborane), 48.05 (1C, $CCH_2CH_2NH_2$), 43.22 (1C, $CCH_2CH_2NH_2$), 37.59 (1C, CCH_2CH_2N); ^{11}B NMR (acetone-d_6, 128.33 MHz): δ = 8.69 (2B, d, J = 141 Hz, B-8, 8́), 0.01 (2B, d, J = 140 Hz, B-10, 10́), –3.9d (6B, d, *overlap*, B-4, 4́, 9, 9́, 12, 12́), –8.50 (2B, d, J = 140 Hz, B-7, 7́), –14.19 (2B, d, J = 125 Hz, B-5, 5́), –15.89 (2B, d, J = 156 Hz B-11, 11́), –20.24 (2B, d, J = 94 Hz, B-6, 6́); UV (95% C_2H_5OH): λ_{min} (nm) = 240, λ_{max} = 278, λ_{sh} = 331; FT-IR: ν_{max} (cm^{-1}) = 3647–3545 (CH arom), 2922, 2852 (CH alkyl), 2544 (BH), 1704, 1659 (C═O), 1599, 1332 (NO_2), 1539, 1508, 1456, 1423 (C═C); ESI-MS: *m/z*: 636.50 (100%), calcd for $C_{20}H_{37}B_{18}CoN_3O_4$: 636.39.

N,Ń-{[2,2′-(3,3′-commo-bis(1,2-dicarba-3-cobalta(III)-closo-dodecaborate-1-yl)ethyl]-1,1′ethyl-}]-(bis(1,8-naphthalimide) (***18***): red solid, yield 129.8 mg (62%). TLC (CH_2Cl_2:CH_3CN 7:1, v/v): R_f = 0.43; ^{1}H NMR (acetone-d_6, 399.98 MHz): δ = 9.34 (2H, s, H-2), 9.05 (2H, s, H-4), 8.72 (2H, t, J = 8.0 Hz, H-7), 8.68 (2H, t, J = 7.8 Hz, H-5), 8.05 (2H, t, J = 7.9, H-6), 4.36 (4H, m, CCH_2CH_2N), 3.89 (2H, br s, CH-carborane), 3.51 (4H, m, CCH_2CH_2N); ^{13}C NMR (acetone-d_6, 100.59 MHz): δ = 163.45 (2C, C═O), 163.05 (2C, C═O), 147.17 (2C,

C-3), 136.78 (2C, C-4), 134.68 (2C, C-7), 132.13 (2C, C-5), 130.87 (2C, C-2), 130.03 (4C, C-10, C-6), 125.16 (2C, C-1), 124.11 (2C, C-9), 123.87 (2C, C-8), 67.80 (2C, CCH_2CH_2N), 59.79 (2C, C-carborane), 58.81 (2C, CH-carborane), 37.82 (2C, CCH_2CH_2N); ^{11}B NMR (acetone-d_6, 128.33 MHz;): δ = 8.94 (2B, d, J = 177 Hz, B-8, 8́), 0.15 (2B, d, J = 140 Hz, B-10, 10́), –4.13 (6B, d, J = 150 Hz, B-4, 4́, 9, 9́, 12, 12́), –8.32 (2B, d, J = 165 Hz, B-7, 7́), –15.14 (4B, d, *overlap*, B-5, 5́,11 11́), –20.51 (2B, d, J = 90 Hz, B-6, 6́); UV (95% C_2H_5OH): λ_{min} (nm) = 241, λ_{max} = 276, λ_{sh} = 330; FT-IR: ν_{max} (cm^{-1}) = 3642–3538 (CH arom), 2921, 2850 (CH alkyl), 2549 (BH), 1704, 1660 (C═O), 1600, 1333 (NO_2), 1541, 1508, 1456, 1423 (C═C); ESI-MS: *m/z*: 860.58 (100%), calcd for $C_{32}H_{41}B_{18}CoN_4O_8$: 862.41.

4.2. Cellular biology

4.2.1. Cytotoxicity assay

The cytotoxic properties of synthesized compounds were evaluated using two human cancer cell lines: RPMI 2650 established from squamous cell carcinoma and HepG2 established from hepatocellular carcinoma. Both cell lines were purchased from Leibniz Institute DSMZ-German Collection of Microorganisms and Cell Cultures (DSMZ, Braunschweig, Germany) and from ECACC (Salisbury, UK).

RPMI 2650 cells were propagated in Minimum Essential Medium (MEM; Life Technologies, Warsaw, Poland) supplemented with 10% heat-inactivated fetal bovine serum (FBS; Life Technologies, Warsaw, Poland), nonessential amino acid solution (NEAA; Life Technologies, Warsaw, Poland) and 100 units/mL penicillin G with 100 mg/mL streptomycin (Life Technologies, Warsaw, Poland). The cells were incubated at 37 °C in a humidified atmosphere containing 5% CO_2.

HepG2 cells were propagated in Dulbecco's Modified Eagle Medium (DMEM; Life Technologies, Warsaw, Poland) supplemented with 10% heat-inactivated fetal bovine serum (FBS; Life Technologies, Warsaw, Poland) and 100 units/mL penicillin G with 100 mg/mL streptomycin (Life Technologies, Warsaw, Poland). The cells were incubated at 37 °C in a humidified atmosphere containing 5% CO_2.

Upon reaching 80–90% confluency, cells were harvested with 0.25% trypsin in 1 mM EDTA (Life Technologies, Warsaw, Poland) and transferred into 96-well microplates at 5000 cells/well (HepG2 cells) or 10,000 cells/well (RPMI 2650 cells). After overnight incubation of cells at 37 °C in a humidified atmosphere containing 5% CO_2, the culture medium was removed and replaced with a freshly prepared solution of compounds in culture medium or medium itself as the control group.

Stock solution of each compound was prepared in DMSO at 50 mM and 25 mM for pinafide. Stock solutions were diluted with the growth medium supplemented with 5% FBS to ensure drug dissolution for obtaining concentrations ranging from 0.1 to 100 μM. The cytotoxicity was evaluated by the MTT assay. The final content of DMSO in solutions did not exceed 0.2%, and an additional control group with 0.2% DMSO was included to rule out the effect of solvent. After treatment, cells were incubated at 37 °C in 5% CO_2 for additional 24 h. Upon completion of the incubation, the medium was aspirated and replaced with 3-(4,5-dimethylthiazol-2-yl)-2,5-diphenyltetrazolium bromide (MTT) dye solution (50 μL, 0.5 mg/mL). After 3 h incubation, the resulting MTT formazan crystals were dissolved in DMSO (100 μL). To ensure the complete dissolution of formazan, the plates were shaken on an orbital microplate shaker at 1000 rpm for 15 min (Thermoshaker NeoLab 7–0055, Bionovo, Poland). The optical density of each well was then measured on a microplate spectrophotometer (Bio-Rad 680; Bio-Rad, Poland) at a wavelength of 570 nm. Each experiment consisted of 5 replications of each concentration, and each experiment was repeated three times independently. The results were calculated as percentage of control group viability. The IC_{50} values were determined using a nonlinear regression from the plot of % viability against log dose of compounds by using GraphPad Prism 6.0 software (GraphPad, San Diego, CA, USA).

4.2.2. Apoptosis/necrosis assay by flow cytometry

Apoptosis/necrosis assay was performed by double staining of cells with YO-PRO-1 (Thermo Fisher Scientific) and propidium iodide (PI, Sigma-Aldrich) fluorescent dyes. Briefly, HepG2 cells (4×10^5) were seeded onto 6-well plates. On the next day, the cells were treated for 24 h with the analyzed compounds at a concentration corresponding to a half of the IC_{50} and whole IC_{50} values. Subsequently, the cells were detached with trypsin (Thermo Fisher Scientific), washed twice with DPBS (1 mL) (Thermo Fisher Scientific), and stained with YO-PRO-1 and PI according to the manufacturer's protocol for 30 min at 37 °C in the dark. The cells were analyzed immediately after staining with 488 nm excitation by Accuri C6 flow cytometer (Becton Dickinson).

4.2.3. Cell cycle analysis by flow cytometry

HepG2 (5×10^5) cells were seeded onto 6-well cell culture plates and incubated for 24 h with the analyzed compounds at a concentration corresponding to a half of the IC_{50} and whole IC_{50} values. DNA content was determined by flow cytometry with PI (Sigma-Aldrich) staining. After incubation, the cells were trypsinized and washed twice with PBS (1 mL). In the next step, the cells were fixed with an ice-cold 80% ethanol. After 1 h incubation in 4 °C, the cells were stored at − 20 °C for further analysis. After double wash with PBS, the fixed cells were stained with PI (50 μg/mL) with the addition of RNAse A (100 μg/mL) for 30 min at 37 °C in the dark. The PI fluorescence was measured by FACSCalibur (Becton Dickinson), and data were analyzed by FlowJo software.

4.2.4. Oxidative stress measurements in HepG2 cells by flow cytometry

HepG2 cells (3.5×10^5) were seeded onto 6-well plates, cultured with EMEM media at 37 °C and 5% CO_2 saturation, and incubated until 60–70% confluence. Subsequently, the cells were treated for 24 h with the tested compounds at a concentration that corresponds to a quarter and a half of IC_{50} value. Next, the cells were detached with trypsin (Sigma-Aldrich) and washed twice with DPBS (1 mL) (Thermo Fisher Scientific), and the level of intracellular ROS generation was analyzed by dual staining with H_2DCFDA/PI according to the manufacturer's protocol (Thermo Fisher Scientific), in which fluorescence was triggered in the presence of ROS.

4.2.5. Analysis of m5C and 8-oxo-dG in HepG2 cells by HPLC-UV-ED

HepG2 cells (1×10^6) were seeded onto flasks (25 cm^2) and cultured in the supplemented growth medium for 16 h. Subsequently, the cells were treated with mitonafide (0.5 μM) or compound **17** (15 μM) for 24 h. After incubation, the cells were trypsinized, rinsed twice with PBS, and pelleted by centrifugation (200*g*, 3 min). Total DNA was isolated from the treated cells and untreated control cells by using Genomic mini DNA isolation kit (A&A Biotechnology) according to the manufacturer's protocol. Quality of the total DNA was assessed spectrophotometrically.

DNA (1 μg) was dissolved in sodium acetate buffer (10 μL, 40 mM, pH 5.3) containing $ZnCl_2$ (0.1 mM) and digested with nuclease *P*1 (3 μg). Samples were incubated for 3 h at 37 °C. Subsequently, Tris-HCl (2 μL, 1 M, pH 8.0) and alkaline phosphatase (1 U) were added and incubated for 2 h at 37 °C. All DNA hydrolysates were ultrafiltered using cutoff 10,000 Da filter units.

m^5dC, dC, 8-oxo-dG, and dG in DNA hydrolysates were determined by HPLC-UV followed by electrochemical detection (Coulochem III Electrochemical Detector ESA, Inc., Chelmsford, MA, USA). DNA hydrolysates were chromatographed isocratically by using ammonium acetate (50 mM, pH 5.3)/methanol (93:7, v/v). Detection of m^5dC and dC was performed at 273 nm, and detection of dG was performed at 254 nm. 8-oxo-dG was determined by the electrochemical detector: guard cell + 400 mV, detector 1: +130 mV (as a screening electrode), detector 2: +350 mV (as a measuring electrode set to sensitivity of 50 nA/V). All results are expressed as mean ± SD.

Amount of modified bases in DNA was calculated on the basis of

genome composition 3.2×10^9 (100%), where $m^5C - 33 \times 10^6$ (1%), G – 663×10^6 (20%).

To determine 8-oxo-dG contents guanosine amount was necessary. The total number of 8-oxo-dG in genome was calculated using special formula.

4.2.6. Immunofluorescence analysis of 8-oxoG/dG

HepG2 cells were seeded at a density of 3.5×10^4 cells/well onto coverslip slides (ø 12 mm) placed in 24-well cell culture dishes in 400 μL of supplemented EMEM. After 24 h, the cells were treated with 15, 20, or 30 μM of compound **17** for the next 24 h. Subsequently, the cells were fixed with 4% formaldehyde for 10 min at RT, permeabilized with 0.5% Triton X-100 in PBS for 5 min at RT, and then blocked in 1% BSA in PBS for 1 h at RT. In the next step, the cells were incubated overnight at 4 °C with primary anti-8-hydroxyguanosine-FITC antibody (Abcam ab183393), and nuclear DNA was then labeled blue with Hoechst 33,342 (3 μg/mL) (Life Technologies) for 5 min. After each step of the procedure, the cells were washed three times with PBS. The fluorescence signal was detected by a Leica TCS SP5 confocal microscope using a Plan Apo 63 × 1.4 NA oil-immersion objective with excitation/emission spectra at 495/515–550 nm for FITC (green fluorescence) and 405/460–500 nm for nuclei visualization (blue fluorescence). Leica LAS AF system software was used for the control of scan process, and Leica LAS X software with 3D deconvolution module was used for image processing and fluorescence analysis.

4.2.7. Confocal microscopy analysis of intracellular and mitochondrial ROS

HepG2 cells were seeded at a density of 6×10^4 cells/well into 4-chamber glass bottom cell culture dishes (Grenier Bio-One) and cultured at 37 °C and 5% CO_2 saturation. After 24 h, cells were treated with compound **17** in the final concentration of 15, 20, or 30 μM. Treated cells were grown for the next 24 h, and the intracellular and mitochondrial ROS was detected using H_2DCFDA (2 μM) (Sigma-Aldrich) and MitoSOX Red Mitochondrial Superoxide Indicator (3 μM) (Life Technologies), respectively. The cells were stained for 30 min (H_2DCFDA) and 15 min (MitoSOX), rinsed with PBS, and placed into prewarmed (37 °C) FluoroBrite DMEM (Thermo Fisher Scientific). Live-cell fluorescence imaging was performed at 37 °C on a Leica TCS SP5 confocal laser scanning microscope with environmental cell culture chamber.

Sequentially scanned images were collected using a Plan Apo 63 × 1.4 NA oil-immersion objective with excitation and emission spectra at 492/510–530 nm for DCF and 510/570–600 nm for MitoSOX reagent. Leica LAS AF software was used for the control of scan process, and LAS X software with 3D deconvolution module was used for image processing and fluorescence analysis.

4.2.8. Flow cytometry analysis of mitochondrial oxidative stress induction

A total of 4×10^5 cells were seeded onto 6-well plates and cultured for 16 h. Subsequently, mitonafide and compound **17** were added to a final concentration of 0.25, 0.5, and 1 μM or 7.5, 15, and 20 μM, respectively, and cultured for 24 h. After incubation, the cells were detached by trypsin and washed with DPBS (1 mL). Cell pellets were stained with MitoSOX (2.5 μM) for 10 min at 37 °C in the dark. The mitochondrial superoxide level was evaluated by flow cytometry analysis.

4.2.9. Statistical analysis

Statistical analyzes were performed using GraphPad Prism version 6.0 for Windows, (GraphPad Software, San Diego, California, USA). Apoptosis and necrosis as well as cell cycle assay was analyzed by two-way analysis of variance (ANOVA), followed by Tukey's multiple comparison test. ROS induction was analyzed by one-way ANOVA followed by Tukey's multiple comparison test. Statistical significance for mitochondrial ROS production was determined by one-way ANOVA followed by Dunnett's multiple comparison test.

The results are presented as mean ± SEM from three independent experiments; p values < 0.05 were considered statistically significant. Statistical significance is indicated with asterisks: (*ns*) $p > 0.05$, (*) $p < 0.05$, (**) $p < 0.01$, (***) $p < 0.001$, and (****) $p < 0.0001$.

4.3. Physicochemical investigation with DNA

4.3.1. Materials

Calf-thymus (ct-DNA) was purchased from Sigma (USA) and used without purification. Sodium cacodylate (for the preparation of cacodylate buffer) was purchased from Acros Organics (Geel, Belgium). Water was obtained from a Milli-Q purification system. All experiments were performed with freshly prepared solutions.

4.3.2. Preparation of ct-DNA

The ct-DNA was dissolved in sodium cacodylate buffer (pH 7.0, 20 mM), reconstituted overnight at 4 °C to dissolve all the material, and then filtered through a 0.45-μm filter. The molar concentration of ct-DNA was determined from UV–visible spectra by using molar absorption coefficient (ε) of 6600 M^{-1} cm^{-1}at 260 nm [52]. The purity of ct-DNA was confirmed by UV–visible spectroscopy by measuring the ratio of absorbance at 260 nm to 280 nm and was found to be ≥1.8, indicating that DNA was sufficiently free of proteins.

4.3.3. Melting temperature (T_m) measurements

The measurements were performed by adding aliquots of DMSO stock solution to the buffer solution (pH 7.0, 20 mM, cacodylate buffer, DMSO content of the final solution = 0.25–0.51%). The T_m curves were collected at r = 0.3 (r = [compound]/[ct-DNA]) to assure the dominant binding mode. Thermal melting curves were determined by following the absorption change at 260 nm as a function of temperature by using a GBC Cintra10 UV–VIS spectrometer (Dandenong, Australia) equipped with a GBC Thermocell Peltier Power Supply (Dandenong, Australia) using a 1-cm path length cell. The absorbance of the samples was monitored at 260 nm from 30 °C to 90 °C with a heating rate of 1 °C/min. T_m values are the midpoints or the transition curves determined from the maximum of the first derivative. The ΔT_m values were calculated by subtracting T_m of the free nucleic acid from T_m of the sample. Every ΔT_m value reported in the study was the average of at least two measurements. The error in ΔT_m was ± 0.5 °C.

4.3.4. Circular dichroism (CD) measurements

The measurements were performed by adding aliquots of DMSO stock solution to the buffer solution (pH 7.0, 20 mM, cacodylate buffer, DMSO content of the final solutions = 0.17–1.3%). Changes in the CD spectrum of ct-DNA upon the addition of compound were measured at different molar ratios r = [compound]/[ct-DNA]. Circular dichroism spectra were recorded on a JASCO J-815 CD spectrometer with JASCO CDF-426S Peltier thermostated cell holder (Tokyo, Japan) by using a rectangular quartz cuvette of path length 0.5 cm (1 mL) in the 230–330 nm region. The reported CD profiles are an average of three successive scans with 200 nm per minute scan time and an appropriately corrected baseline. The temperature was maintained at 25 °C during the experiment.

Declaration of Competing Interest

The authors declare that they have no known competing financial interests or personal relationships that could have appeared to influence the work reported in this paper.

Acknowledgements

This study was supported by the National Science Centre, Poland, Grant No. 2014/14/E/ST5/00577 (A.B.O, D.R, S.R), and Czech Science

Foundation, Czech Republic, Project No. 18-27648 (J.N, B.G). The contribution from the Statutory Fund of IMB PAS is also gratefully acknowledged. A CombiFlash PurIon Model Eurus35 (Teledyne ISCO, Lincoln, USA) was purchased from Grant No. 2014/14/E/ST5/00577.

Appendix A. Supplementary material

Supplementary data to this article can be found online at https://doi.org/10.1016/j.bioorg.2019.103432. These data include ^{1}H, ^{13}C, ^{11}B, $^{11}B\{H\}$ NMR, FT-IR, MS, CD spectra of compound **3**, **5**, **7**, **9**, **11**, **13**, **15**, **17**, **18**, flow cytometry analysis of apoptosis/necrosis, cycle distribution, ROS production in HepG2 cells.

References

[1] A. Kamal, N.R. Bolla, P.S. Srikanth, A.K. Sirvastava, Naphthalimide derivatives with therapeutic characteristics: a patent review, Expert Opin. Ther. Pat. 23 (2013) 299–317.
[2] R. Tandon, V. Luxami, H. Kaur, N. Tandon, K. Paul, 1,8-Naphthalimide: a potent DNA intercalator and target for cancer therapy, Chem. Rec. 17 (2017) 1–39.
[3] K. Shen, L. Sun, H. Zhang, Y. Xu, X. Qian, Y. Lu, Q. Li, L. Ni, J. Liu, A ROS-mediated lysosomal-mitochondrial pathways is induced by a novel Amonafide analogue, 7c, in human HeLa cervix carcinoma cells, Cancer Lett. 333 (2013) 229–238.
[4] G.H. Su, T.A. Sohn, B. Ryu, S.E. Kern, A novel histone deacetylase inhibitor identified by high-throughput transcriptional screening of a compound library, Cancer Lett. 60 (2000) 3137–3142.
[5] A. Pain, S. Samanta, S. Dutta, A.K. Saxena, M. Shanmugavel, H. Kampasi, G.N. Quazi, U. Sanyula, Synthesis and evaluation of substituted naphthalimide nitrogen mustards as rationally designed anticancer compound, Acta Pol. Pharm. 60 (2003) 285–291.
[6] J. Shao, Y. Li, Z. Wang, M. Xiao, P. Yin, Y. Lu, X. Qian, Y. Xu, J. Liu, 7b, a novel naphthalimide derivative, exhibited anti-inflammatory effects via targeted-inhibiting TAK-1 following down-regulation of ERK1/2- and p38 MAPK-mediated activation of NF-κB in LPS-stimulated RAW264.7 macrophages, Int. Immunopharmacol. 17 (2013) 216–228.
[7] S. Banerjee, E.B. Veale, C.M. Phelan, S.A. Murphy, G.M. Tocci, L.J. Gillespie, D.O. Frimannsson, J.M. Kelly, T. Gunnlaugsson, Recent advances in the development of 1,8-naphthalimide based DNA targeting binders, anticancer and fluorescent cellular imaging agents, Chem. Soc. Rev. 42 (2013) 1601–1618.
[8] M.F. Brana, A. Ramos, Naphthalimides as anticancer agents: synthesis and biological activity, Curr. Med. Chem. Anticancer Agents 1 (2001) 237–255.
[9] M. Lv, H. Xu, Overview of naphthalimide analogs as anticancer agents, Curr. Med. Chem. 16 (2009) 4797–4813.
[10] C. Ge, L. Chang, Y. Zhao, C. Chang, X. Xu, H. He, Y. Wang, F. Dai, S. Xie, C. Wang, Design, synthesis and evaluation of naphthalimide derivatives as potential anticancer agents for Hepatocellular Carcinoma, Molecules 22 (2017) 342, https://doi.org/10.3390/molecules22020342.
[11] M.D. Tomczyk, K.Z. Walczak, 1,8-Naphthalimide based DNA intercalators and anticancer agents. A systematic review from 2007 to 2017, Eur. J. Med. Chem. 159 (2018) 393–422.
[12] J. Kahlert, C.J.D. Austin, M. Kassiou, L.M. Rendina, The fifth element in drug design: boron in medicinal chemistry, Aust. J. Chem. 66 (2013) 1118–1123.
[13] L. Ciani, S. Ristori, Boron as a platform for new drug design, Expert Opin. Drug Dis. 7 (2012) 1017–1027.
[14] M. Scholz, E. Hey-Hawkins, Carbaboranes as pharmacophores: properties, synthesis and application strategies, Chem. Rev. 111 (2011) 7035–7062.
[15] F. Issa, M. Kassiou, L.M. Rendina, Boron in drug discovery: carboranes as unique pharmacophores in biologically active compounds, Chem. Rev. 111 (2011) 5701–5722.
[16] Z.J. Leśnikowski, Challenges and opportunities for the application of boron clusters in drug design, J. Med. Chem. 59 (2016) 7738–7758.
[17] Z.J. Leśnikowski, Recent developments with boron as a platform for novel drug design, Expert Opin. Drug Dis. 11 (2016) 569–578.
[18] T.M. Goszczyński, K. Fink, J. Boratyński, Icosahedral boron clusters as modifying entities for biomolecules, Expert Opin. Drug. Dis. 18 (2018) 205–213.
[19] E. Hey-Hawkins, C. Vinas Teixidor, Boron-based Compounds: Potential and Emerging Applications in Medicine, first ed., John Wiley & Sons Ltd, Oxford, 2018.
[20] P. Cigler, M. Kožišek, P. Řezáčová, J. Brynda, Z. Otwinowski, J. Pokorná, J. Plešek, B. Grüner, L. Dolečková-Marešová, M. Máša, J. Sedláček, J. Bodem, H.-G. Kräusslich, V. Kral, J. Konvalinka, From nonpeptid toward noncarbon protease inhibitors: metallacarboranes as specific and potent inhibitors of HIV protease, PNAS 102 (2005) 15394–115299.
[21] P. Řezáčová, J. Pokorná, J. Brynda, M. Kožišek, P. Cigler, M. Lepsik, J. Fanfrlik, J. Řezáč, K. Grantz Šašková, I. Sieglová, J. Plešek, V. Šicha, B. Grüner, H. Oberwinkler, J. Sedláček, H.-G. Kräusslich, P. Hobza, V. Kral, J. Konvalinka, Design of HIV protease inhibitors, on inorganic polyhedral metallacarboranes, J. Med. Chem. 52 (2009) 7132–7141.
[22] H. Ghaneolhosseini, S. Sjöberg, Synthesis of a boronated naphthalimide for potential use in Boron Neutron Capture Therapy (BNCT), Acta Chem. Scand. 53 (1999) 298–300.
[23] S. Ghirmai, J. Malmquist, H. Lundquist, V. Tolmachev, S. Sjöberg, Synthesis and radioiodination of 7-(3′-ammoniopropyl)-7,8-dicarba-*nido*-undecabroate(-1), (ANC), J. Labeled Compd. Rad. 47 (2004) 557–569.
[24] E. Kvasničková, J. Masák, J. Čejka, O. Matátková, V. Šicha, Preparation, characterization, and the selective antimicrobial activity of N-alkylammonium 8-diethyleneglycol cobalt bis-dicarbollide derivatives, J. Organomet. Chem. 827 (2017) 23–31.
[25] J. Nekvinda, J. Švehla, I. Císařová, B. Grüner, Chemistry of cobalt bis(1,2-dicarbollide ion); the synthesis of carbon substituted alkylamino derivatives from hydroxyalkyl derivatives *via* methylsulfonyl or p-toluenesulfonul esters, J. Organomet. Chem. 798 (2015) 112–120.
[26] H.K. Agarwal, B. Buszek, K.G. Ricks, W. Tjarks, Synthesis of closo-1,7-carboranyl alkyl amines, Tetrahedron Lett. 52 (2011) 5664–5667.
[27] A.B. Olejniczak, B. Grüner, V. Šícha, S. Broniarek, Z.J. Leśnikowski, Metallacarboranes as Labels for Multipotential Electrochemical Coding of DNA [8-Dioxane-3-chromium bis(dicarbollide)]^{0} and its nucleoside conjugates, Electroanalysis 21 (2009) 501–506.
[28] A.L. Spek, PLATON SQUEEZE: a tool for the calculation of the disordered solvent contribution to the calculated structure factors, Acta Crystallogr. C 71 (2015) 9–18.
[29] T. Mosmann, Rapid colorimetric assay for cellular growth and survival: application to proliferation and cytotoxicity assays, J. Immunol. Methods 65 (1983) 55–63.
[30] K. Berg, M.B. Hansen, S.E. Nielsen, A new sensitive bioassay for precise quantification of interferon activity as measured via the mitochondrial dehydrogenase function in cells (MTT-method), APMIS 98 (1990) 156–162.
[31] S.Q. Xie, Q. Li, Y.H. Zhang, J.H. Wang, Z.H. Mei, J. Zhao, C.J. Wang, NPC-16, a novel naphthalimide-polyamine conjugate, induced apoptosis and autophagy in human hepatoma HepG2 cells and Bel-7402 cells, Apoptosis 16 (2011) 27–34.
[32] Z. Chen, X. Liang, H. Zhang, H. Xie, J. Liu, Y. Xu, W. Zhu, Y. Wang, X. Wang, S. Tan, A new class of naphthalimide-based antitumor agents that inhibit topoisomerase II and induce lysosomal membrane permeabilization and apoptosis, J. Med. Chem. 53 (2010) 2589–2600.
[33] L. Ji, S. Yang, S. Li, S. Liu, S. Tang, Z. Liu, X. Meng, S. Yu, A novel triazolo-naphthalimide induces apoptosis and inhibits tumor growth by targeting DNA and DNA-associated processes, Oncotarget 8 (2017) 37394–37408.
[34] T. Chen, P.A. Stephens, F.K. Middleton, N.J. Curtin, Targeting the S and G2 checkpoint to treat cancer, Drug Discov. Today 17 (2012) 194–202.
[35] Y. Dabiri, A. Schmid, J. Theobald, B. Blagojevic, W. Streciwilk, I. Ott, S. Wölfl, X. Cheng, A Ruthenium(II) N-heterocyclic carbene (NHC) complex with naphthalimide ligand triggers apoptosis in colorectal cells via activating the ROS-p38 MAPK pathway, Int. J. Mol. Sci. 19 (2018) 3964, https://doi.org/10.3390/ijms19123964.
[36] P.C. Hanawalt, Genomic instability: Environmental invasion and the enemies within, Mutat. Res. 400 (1998) 117–125.
[37] D.E. Barnes, T. Lindahl, Repair and genetic consequences of endogenous DNA base damage in mammalian cells, Annu. Rev. Genet. 38 (2004) 445–476.
[38] H. Kasai, S. Nishimura, Hydroxylation of deoxyguanosine at the C-8 position by ascorbic acid and other reducing agents, Nucleic Acids Res. 12 (1984) 2137–2145.
[39] S. Shibutani, M. Takeshita, A.P. Grollman, Insertion of specific bases during DNA synthesis past the oxidation-damaged base 8-oxo-dG, Nature 349 (1991) 431–434.
[40] L.D. Moore, T. Le, G. Fan, DNA methylation and its basic function, Neuropsychopharmacology 38 (2013) 23–38.
[41] I. Shokolenko, N. Venediktova, A. Bochkareva, G.L. Wilson, M.F. Alexeyev, Oxidative stress induces degradation of mitochondrial DNA, Nucleic Acids Res. 37 (2009) 2539–2548.
[42] S.S. Wijeratne, J.M. Patel, C.H. Kiang, Melting transitions of DNA-capped gold nanoparticle assemblies, Springer, New York, NY, 2012, pp. 269–282.
[43] J.L. Mergny, G. Duval-Valentin, C.H. Nguyen, L. Perrouault, B. Faucon, M. Rougee, T. Montenay Garestier, E. Bisagni, C. Helene, Triple helix-specific ligands, Science 256 (1992) 1681–1684.
[44] E.A. Lesnik, C.J. Guinosso, A.M. Kawasaka, H. Sasmor, M. Zounes, L.L. Cummins, D.J. Ecker, P.D. Cook, S.M. Freier, Oligonucleotides containing 2′-O-modified adenosine: synthesis and effects on stability of DNA:RNA duplex, Biochemistry 32 (1993) 7832–7838.
[45] V.I. Ivanov, L.E. Minchenkova, A.K. Schyolkina, A.I. Poletayev, Different conformations of double-stranded nucleic acids in solution as revealed by circular dichroism, Biopolymers 12 (1973) 89–110.
[46] H. Jiang, L. Shang, Z.X. Wang, S.J. Dong, Spectrometric and voltammetric investigation of interaction of neutral red with calf thymus DNA: pH effect, Biophys. Chem. 118 (2005) 42–50.
[47] B. Önfelt, P. Lincoln, B. Norden, Enantioselective DNA threading dynamics by phenazine-linked [Ru(phen)$_2$d ppz^{12}+ dimers, J. Am. Chem. Soc. 123 (2001) 3630–3637.
[48] Q. Yang, P. Yang, X. Qian, L. Tong, Naphthalimide intercalators with chiral amino side chains: effects of chirality on DNA binding, photodamage and antitumor cytotoxicity, Bioorg. Med. Chem. Lett. 18 (2008) 6210–6213.
[49] Methods in Enzymology, Macromolecular Crystallography, Part A vol. 276, (1997) 307–326.
[50] G.M. Sheldrick, SHELXT-Integrated space-group and crystal-structure determination, Acta Crystallogr. A A71 (2015) 3–8.
[51] G.M. Sheldrick, A short history of SHELX, Acta Crystallogr. A 64 (2008) 112–122.
[52] Y. Egawa, R. Hayashida, T. Seki, J. Anzai, Fluorometric determination of heparyn based on self-quenching of fluorescein-labeled protamine, Talanta 76 (2008) 736–741.